Graduate School ETD Form 9
(Revised 12/07)

PURDUE UNIVERSITY
GRADUATE SCHOOL
Thesis/Dissertation Acceptance

This is to certify that the thesis/dissertation prepared

By David Robert Sempsrott

Entitled
Analysis of the Bioelectric Impedance of the Tissue-Electrode Interface Using a Novel Full-Spectrum Approach

For the degree of Master of Science in Biomedical Engineering

Is approved by the final examining committee:

Ken Yoshida
Chair

Edward Berbari

Paul Salama

To the best of my knowledge and as understood by the student in the *Research Integrity and Copyright Disclaimer (Graduate School Form 20)*, this thesis/dissertation adheres to the provisions of Purdue University's "Policy on Integrity in Research" and the use of copyrighted material.

Approved by Major Professor(s): Ken Yoshida

Approved by: Edward Berbari 11/20/12
Head of the Graduate Program Date

المنارة للاستشارات
www.manaraa.com

Graduate School Form 20
(Revised 9/10)

PURDUE UNIVERSITY
GRADUATE SCHOOL

Research Integrity and Copyright Disclaimer

Title of Thesis/Dissertation:

Analysis of the Bioelectric Impedance of the Tissue-Electrode Interface Using a Novel Full-Spectrum Approach

For the degree of Master of Science in Biomedical Engineering

I certify that in the preparation of this thesis, I have observed the provisions of *Purdue University Executive Memorandum No. C-22,* September 6, 1991, *Policy on Integrity in Research.**

Further, I certify that this work is free of plagiarism and all materials appearing in this thesis/dissertation have been properly quoted and attributed.

I certify that all copyrighted material incorporated into this thesis/dissertation is in compliance with the United States' copyright law and that I have received written permission from the copyright owners for my use of their work, which is beyond the scope of the law. I agree to indemnify and save harmless Purdue University from any and all claims that may be asserted or that may arise from any copyright violation.

David Robert Sempsrott

Printed Name and Signature of Candidate

11/30/2012

Date (month/day/year)

*Located at http://www.purdue.edu/policies/pages/teach_res_outreach/c_22.html

المنارة للاستشارات
www.manaraa.com

ANALYSIS OF THE BIOELECTRIC IMPEDANCE OF THE TISSUE-ELECTRODE INTERFACE USING A NOVEL FULL-SPECTRUM APPROACH

A Thesis

Submitted to the Faculty

of

Purdue University

by

David Robert Sempsrott

In Partial Fulfillment of the

Requirements for the Degree

of

Master of Science in Biomedical Engineering

December 2012

Purdue University

Indianapolis, Indiana

المنارة للاستشارات

www.manaraa.com

To the great Engineer who designed all the intricacies of the systems I have studied,

granted me the ability to study them. . .

and loved me enough to die for me while I was His enemy.

To my Lord Jesus Christ be all glory and honor for this thesis.

المنارة للاستشارات

www.manaraa.com

ACKNOWLEDGMENTS

As any research project should be, this work has been both challenging and rewarding, both theoretical and practical. I am truly grateful for the opportunity to be involved in this research and for all the individuals who have supported me in this work, either by contributing to the project or by keeping me (mostly) sane during the project.

In particular, I would like to thank my major professor, Dr. Ken Yoshida, for providing me with the opportunity to work in his lab and for the the ideas, guidance, and financial support to complete this project. (Ken, you may not know this, but I heard about Cyberhand in high school and it was the dream of working on a project like Cyberhand that propelled me into biomedical engineering. Little did I know I would one day work in the lab of a key Cyberhand researcher. Thanks for helping me realize a dream.) I would also like to thank the other members of my advisory committee, Dr. Edward Berbari and Dr. Paul Salama, for their support and oversight. Additional thanks go to my fellow researchers in Europe, specifically Dr. Michael Grey who led the experimental efforts and Mark van de Ruit who executed the Birmingham trials. Thanks to my parents, grandparents, brothers, and sister who made home a haven and always encouraged and prayed for me. My appreciation also goes to all my colleagues at the bioelectronics lab at IUPUI, especially Shaoyu Qiao and Kevin Mauser who provided valuable advice, encouragement, and friendship throughout the duration of this project. Thanks to Knud Larsen at Aalborg University for the use of his original software libraries for exporting LabVIEW data to MATLAB format, a key component of our impedance recording application. Finally, I gratefully acknowledge financial support for this work from the IUPUI University Fellowship, an assistantship at the Department of Biomedical Engineering at IUPUI, and a grant from the Hede Nielsen Family Foundation in Denmark.

المنارة للاستشارات
www.manaraa.com

TABLE OF CONTENTS

Page

LIST OF TABLES vii

LIST OF FIGURES viii

LIST OF SYMBOLS x

ABSTRACT xi

1 INTRODUCTION 1
1.1 Background and Prior Work 2
1.2 Overview of Current Work 6
1.2.1 Development of Impedance Analysis System 6
1.2.2 Experimental Application of Measurement System to Skin Impedance and EMG Analysis 7
1.3 Organization of the Thesis 8
1.3.1 Chapter 2: Mathematical Models of Bioimpedance 8
1.3.2 Chapter 3: Software Implementation and Validation of the Cole Models 8
1.3.3 Chapter 4: Development of the Impedance Analysis System . . . 9
1.3.4 Chapter 5: Analysis of the Effects of Skin Preparation Methods on Tissue-Electrode Interface Impedance and sEMG Recordings . . 9

2 MATHEMATICAL MODELS OF BIOIMPEDANCE 10
2.1 Series Models 10
2.2 Parallel Models 12
2.3 Series-Parallel Relationships in the Simple Linear RC Circuit 14
2.3.1 Capacitance 14
2.3.2 Time Constant 15

3 SOFTWARE IMPLEMENTATION AND VALIDATION OF THE COLE MODELS 17
3.1 Method 17
3.1.1 Input 17
3.1.2 Algorithm 17
3.2 Experimental Validation 19
3.3 Results 20
3.4 Discussion and Conclusions 21

المنارة للاستشارات

www.manaraa.com

Page

4 DEVELOPMENT OF THE IMPEDANCE ANALYSIS SYSTEM 23
4.1 Stimulation/Sensing Hardware 23
4.2 Impedance Acquisition/Calculation Software 25
4.3 Post-Hoc Impedance Data Processing Software 29
4.4 Summary 31

5 ANALYSIS OF THE EFFECTS OF SKIN PREPARATION METHODS ON TISSUE-ELECTRODE INTERFACE IMPEDANCE AND SEMG RECORDINGS 32
5.1 Introduction 32
5.2 Methods 33
5.2.1 Participants 33
5.2.2 Skin Preparation 33
5.2.3 Spectral Characterization of Tissue-Electrode Interfacial Impedance 34
5.2.4 SNR Validation Using sEMG 36
5.2.5 Noise Immunity Test 37
5.3 Results 37
5.3.1 Impedance Tests 38
5.3.2 SNR Tests 39
5.3.3 Noise Immunity Tests 39
5.4 Discussion 39
5.5 Conclusion 43

6 SUMMARY 44

LIST OF REFERENCES 47

APPENDICES

A RAPID MEASUREMENT OF COMPLEX IMPEDANCE SPECTRA OF ELECTRODES 50
A.1 Introduction 50
A.2 Methods 52
A.2.1 Technique 52
A.2.2 Testing and Validation 53
A.3 Results 55
A.4 Discussion 58
A.5 Conclusion 61

B CALIBRATION AND COMPENSATION FOR LEAD WIRE PARASITIC CAPACITANCE 63
B.1 Introduction 63
B.2 Technique 65
B.3 Validation 66

المنارة للاستشارات
www.manaraa.com

Page

B.4 Results 66
B.5 Discussion 67
B.6 Conclusion 68

المنارة للاستشارات
www.manaraa.com

LIST OF TABLES

Table Page

3.1 RC test circuit component/characteristic values 19

3.2 RC test circuit values calculated by Cole algorithm 21

5.1 Skin preparation methods 34

المنارة للاستشارات

www.manaraa.com

LIST OF FIGURES

Figure Page

2.1 A simple resistor-capacitor network as a rough approximation to tissue impedance. 11

2.2 The Cole impedance system. 12

2.3 The parallel version of the simple resistor-capacitor network. 13

2.4 The Cole admittance system. 13

3.1 RC circuit impedance data fitted to the Cole_Z (left) and Cole_Y (right) circuit models. Acquired data are shown in blue with the fitted curve in green, and the centroid is marked in red. Parameter values extracted from the fit are shown at the top of each graph. 21

3.2 Tissue-electrode impedance data fitted to the Cole_Z circuit model. The centroid (marked in red at the top of the plot window) is located beyond the real axis with respect to the data, as predicted by the model. 22

4.1 Functional pseudo-circuit block diagram of the noise stimulation/sensing circuit. Shaded blocks indicate components not integrated into the hardware design but connected via the integrated BNC jacks. 24

4.2 Design process view of the stimulation/sensing hardware, including circuit schematic, PCB layout, and photo of completed product. 26

4.3 Comparison of estimates of parasitic capacitance in the measurement apparatus using the previous and updated hardware revisions. 27

4.4 Screenshot of cImp 1.0, the updated release of the acquisition/calculation software. The virtual oscilloscope is shown together with the main window and the recording popup, with a view of the code in the background. 28

4.5 Screenshot of cImpAnalysis. An example data set has been loaded into the plot area. 29

5.1 Typical arrangement of electrode pairs on patches of skin. Labels added for clarity. 35

المنارة للاستشارات

www.manaraa.com

Figure Page

5.2 Schematic breakdown of measured impedance Z_m. In order to obtain the impedance of the tissue-electrode interface, Z_m must be compensated for (1) the parasitic capacitance C_p of the lead cables through the air, (2) the internal impedance of both electrodes, and (3) the resistance of deeper tissue between the electrodes, assumed equal to R_∞ [24]. 35

5.3 An example data set with impedance and sEMG recordings. 38

5.4 Aggregate mean results over all data sets for each preparation type. Error bars represent 95% confidence intervals. The Fisher LSD for pairwise means comparisons among preparation types is shown in red. These results demonstrate that abrasive preparations correlate to lower impedance and higher SNR. . . . 40

5.5 Raw recording example and aggregate mean results for the noise immunity tests. These demonstrate both graphically and statistically that abrasive preparations correlate to substantially increased immunity to induced noise. . . . 41

Appendix Figure

A.1 Magnitude and phase of impedance recorded from a simple RC filter (10 kΩ || 0.1 μF) using two modes of broad bandwidth current, frequency sweep (black) and broad bandwidth noise (dashed). These are shown compared to the theoretical curves (gray). 56

A.2 Magnitude and phase of the impedance recorded from a cuff electrode in saline using the noise method. 57

A.3 Magnitude and phase of the impedance recorded from a cuff electrode implanted acutely around the sciatic nerve of an anesthetized rabbit. Impedance was characterized using both modes of broad bandwidth current, frequency sweep (black) and broad bandwidth noise (dashed). 57

A.4 Frequency profiles of impedance recorded from the calibrated resistor set. The dominance of the parasitic capacitance at higher impedances and frequencies is demonstrated by the divergence of compensated and uncompensated profile pairs and the convergence of all uncompensated profiles to the same asymptote as frequency increases. 58

A.5 Colormaps showing relative percent errors in measurements of impedance magnitude (top) and phase (bottom), as a function of impedance and frequency for the calibrated resistor set. 59

A.6 Frequency profiles of capacitance recorded from the calibrated capacitor set. 60

B.1 Calibration and compensation performed by the described methods. 67

المنارة للاستشارات
www.manaraa.com

LIST OF SYMBOLS

Z	impedance
Y	admittance
R	resistance
R_0	resistance at zero frequency
R_∞	resistance at infinite frequency
C	capacitance
τ	time constant
ω	angular frequency
j	imaginary operator, equivalent to $\sqrt{-1}$
$\Re$	real part
$\Im$	imaginary part

المنارة للاستشارات
www.manaraa.com

ABSTRACT

Sempsrott, David R. M.S.B.M.E., Purdue University, December 2012. Analysis of the Bioelectric Impedance of the Tissue-Electrode Interface Using a Novel Full-Spectrum Approach. Major Professor: Ken Yoshida.

Non-invasive surface recording of bioelectric potentials continues to be an essential tool in a variety of research and medical diagnostic procedures. However, the integrity of these recordings, and hence the reliability of subsequent analysis, diagnosis, or recommendations based on the recordings, can be significantly compromised when various types of noise are allowed to penetrate the recording circuit and contaminate the signals. In particular, for bioelectric phenomena in which the amplitude of the biosignal is relatively low, such as muscle activity (typically on the order of millivolts) or neural traffic (microvolts), external noise may substantially contaminate or even completely overwhelm the signal. In such circumstances, the tissue-electrode interface is typically the primary point of signal contamination since its impedance is relatively high compared to the rest of the recording circuit. Therefore, in the recording of low-amplitude biological signals, it is of paramount importance to minimize the impedance of the tissue-electrode interface in order to consistently obtain low-noise recordings.

The aims of the current work were (1) to complete the development of a set of tools for rapid, simple, and reliable full-spectrum characterization and analytical modeling of the complex impedance of the tissue-electrode interface, and (2) to characterize the interfacial impedance and signal-to-noise ratio (SNR) at the surface of the skin across a variety of preparation methods and determine a factor or set of factors that contribute most effectively to the reduction of tissue-electrode impedance and noise contamination during recording. Specifically, we desired to test an initial hypothesis that surface abrasion is the principal

المنارة للاستشارات
www.manaraa.com

determining factor in skin preparation to achieve consistently low-impedance, low-noise recordings.

During the course of this master's study, (1) a system with portable, battery-powered hardware and robust acquisition/analysis software for broadband impedance characterization has been achieved, and (2) the effects of skin preparation methods on the impedance of the tissue-electrode interface and the SNR of surface electromyographic recordings have been systematically quantified and compared in human subjects. We found our hypothesis to be strongly supported by the results: the degree of surface abrasion was the only factor that could be correlated to significant differences in either the interfacial impedance or the SNR. Given these findings, we believe that abrasion holds the key to consistently obtaining a low-impedance contact interface and high-quality recordings and should thus be considered an essential component of proper skin preparation prior to attachment of electrodes for recording of small bioelectric surface potentials.

المنارة للاستشارات
www.manaraa.com

1. INTRODUCTION

Non-invasive surface recording of bioelectric potentials continues to be an essential tool in a variety of research and medical diagnostic procedures. From routine cardiac monitoring to investigative polygraph tests, the biopotentials obtained from surface recordings offer invaluable insight into the complex physiological processes that give rise to both normal and pathological phenomena. However, the integrity of these recordings, and hence the reliability of subsequent analysis, diagnosis, or recommendations based on the recordings, can be significantly compromised when various types of noise are allowed to penetrate the recording circuit and contaminate the signals.

The severity of this problem varies widely depending on the type of recording attempted, the electrodes used, the bioelectric impedance of the tissue-electrode interface, the recording location, and other factors. In situations where the biosignal to be recorded is relatively large in amplitude, most noise sources can be ignored as their effect will be small. But for bioelectric phenomena in which the amplitude of the biosignal is relatively low, such as EMG (typically on the order of millivolts) or neural traffic (microvolts), external noise may substantially contaminate or even completely overwhelm the signal.

In such circumstances, the tissue-electrode interface is typically the primary point of signal contamination since its impedance is relatively high compared to the rest of the recording circuit. Therefore, in the recording of low-amplitude biological signals, it is of paramount importance to minimize the impedance of the tissue-electrode interface in order to consistently obtain low-noise recordings. Accordingly, the primary aim of the present work was to quantitatively assess the effects of different methods of skin preparation, comparing both the impedances and the signal-to-noise ratios obtained with the respective preparation methods, and to determine a factor or set of factors that contribute

المنارة للاستشارات
www.manaraa.com

most effectively to the reduction of tissue-electrode impedance and noise contamination during recording.

Concurrent with this primary aim was a desire to develop a practical system to measure the frequency-dependent nature of the impedance of tissues, electrodes, and their interfacial regions. Historically impedance has often been measured at only one frequency [1]; although this may be sufficient for some applications, it nevertheless provides a very incomplete picture of the electrical nature of biological tissue and its behavior (discussed further in Appendix A). Therefore, a second aim of the present work was to complete the development of a practical system for simultaneous measurements of impedance over a wide spectrum of frequencies. Because a substantial portion of the development, including prototypes of the measurement system, had already been completed, and the work undertaken during this master's study consisted principally of refining the systems and algorithms already under development, most of this work is not covered in detail in the thesis itself (with the exception of the Cole analysis algorithm, covered in Chapter 3). Instead, details of the development and testing of the hardware apparatus is contained in Appendix A, and a separate effort involving calibration and compensation for internal distortion of measurements is covered in Appendix B. An overview of the contributions made during the present master's study is provided later in this chapter, with some further elaboration in Chapter 4.

1.1 Background and Prior Work

Much of the early work on analysis of bioimpedance and its frequency-dependent characteristics began to be published in the 1920s and 1930s. Kenneth S. Cole, Hugo Fricke, and other contemporaries quantified the resistive and capacitive properties of biological tissue, demonstrating that the impedance could be approximately modeled in the form of RC circuits [2–4]. Cole explained the impedance of cellular suspensions both theoretically [2] using Maxwell's derivations for resistance of concentric spheres, and experimentally [3] using data from his investigations of sea urchin eggs.

المنارة للاستشارات
www.manaraa.com

These early works also noted that the capacitance of most biological tissues is not frequency-independent but varies with frequency as a power law [3]. This leads to a shift of the impedance profile in the complex plane, and makes the impedance impossible to model accurately with purely linear circuit components. Cole continued to investigate this nonlinear behavior, noting that the phase angle of the capacitance seemed to be constant for a given tissue [2] but varied across tissue types [5]. Eventually, in 1940, Cole presented an equation that captured the power-law relationship of the frequency dependence [6]. The Cole equation will be discussed in more detail in Chapter 2 as it forms the basis for the impedance analysis performed in the present work.

As the impedance behavior of biological tissues began to be better understood, it became evident that problems with noise corrupting the ECG and other types of biopotential recordings were related to the electrical properties of the tissues and/or electrodes, specifically the impedance. In 1975, for example, Gordon analyzed triboelectric noise (artifacts arising from static electric charge activity) in ECG and demonstrated that the noise was correlated to the impedance of the tissue-electrode interface [7]. By 1977, Tam and Webster stated that it was "well accepted that skin abrasion improves the quality of biopotential recording by minimizing skin impedance" although the question of exactly how to provide sufficient abrasion without undue discomfort or tissue damage remained a subject of some controversy [8]. Nevertheless, the necessity of providing some method to remove or heavily compromise the high-impedance layer of the skin seems to have been well established by this point. Sandpaper, scouring pads, micropuncture, and/or electrolytic pastes and gels are methods that have since been used or suggested [9–13]. The abrasion paradigm even became commercialized: in 1981 Quinton Instrument Co. patented [14] an automatic abrasion device that rotated an abrasive pad while continuously monitoring the tissue-electrode impedance until the impedance dropped below a predetermined threshold or the device timed out.

However, despite such general acceptance at that time, more recently the importance of abrasion to ensure sufficient compromise of the high-impedance skin barrier seems to have been forgotten to a significant extent. Whereas sandpaper or other abrasives were used

المنارة للاستشارات
www.manaraa.com

earlier, recently more non-abrasive methods — or even minimal or no preparation at all — have begun to be preferred. In 2000, the European concerted action SENIAM reviewed the contemporary (1991 and thereafter) European literature on surface electromyography and reported a lack of consensus not only on preferred methods of skin preparation, but also on whether it was even necessary to abrade the skin at all. The review found that many authors did not even indicate whether they prepared the skin in any way. In view of these findings, SENIAM recommended merely cleaning the skin with alcohol and shaving if necessary [13].

Given the historical reliance on abrasion to reduce impedance and improve recording quality, and the seeming lack of published justification for departure from the abrasion paradigm, this trend is puzzling. However, it may be partially explained by assumptions regarding improvements in amplifier technology. As recording technology has progressed, recording amplifiers have increased in input impedance and in common-mode rejection ratio (CMRR). For example, vacuum-tube amplifiers, used in early recording systems, have relatively low input impedance on the order of 50 kΩ [15], or in the general range of our calculated values for galvanic skin impedance. This made accurate recordings difficult since nearly as much voltage drop appears across the load as across the amplifier. As integrated circuits began to replace vacuum-tube technology, op-amps with bipolar-junction transistor (BJT) inputs began to be used for recording; these had moderately high input impedances on the order of 2 MΩ [16]. In contrast, a common instrumentation amplifier in current technology, the INA111, has field-effect transistor (FET) inputs yielding a nominal input impedance on the order of 10^{12} Ω, and laser-trimmed matching resistors improving the CMRR to over 100 dB [17]. These characteristics have allowed recording systems to substantially increase in accuracy and precision, and it would be easy to assume that this progress in recording technology renders careful skin treatment obsolete. According to this reasoning, impedance mismatch was a concern when the amplifier and the load were on the same order, but it's not a concern now that they are separated by many orders of magnitude. However, input impedance and CMRR alone are not the whole story.

المنارة للاستشارات
www.manaraa.com

In addition to these two input characteristics of the recording amplifier, a third factor affecting the recording quality is the impedance balance between the input electrodes. Merletti *et al.* rightly point out that a significant impedance imbalance at the electrodes can cause a common-mode signal such as power line noise to be converted to a differential-mode signal and captured in the recording even if the internal CMRR of the amplifier is high [18]. As we found in the present experiments (Chapter 5), the tissue-electrode interface impedance of unprepared skin can apparently exceed 100 kΩ; thus, if the electrode impedances are not well balanced, the recording circuit may suffer from impedance mismatch and low common-mode rejection characteristics. In addition, phase differences between separate tissue-electrode interfaces can lead to significant artifacts; this will be discussed further in the context of our experimental results.

The present study was undertaken with a critical view of the departure from abrasion as a necessary component of skin preparation to achieve clean biopotential recordings. In agreement with the earlier publications summarized above, we hypothesize that without the substantial disruption of the stratum corneum effected by surface abrasion, low interfacial impedance and good signal integrity cannot be consistently attained. The present study proposed to test our hypothesis by quantitatively comparing the impedance of the tissue-electrode interface and measured signal-to-noise ratio of biopotential recordings across a variety of abrasive and non-abrasive skin preparation methods.

In order to obtain comprehensive impedance characteristics of the tissue-electrode interface noninvasively, a full-spectrum impedance characterization and analysis system was developed. The system consists of custom-designed hardware to produce broadband noise excitation and monitor tissue response at all frequencies simultaneously, as well as custom software to calculate impedance profiles from the response data and fit the calculated impedance to the Cole models. Preliminary forms of this development [19] as well as the skin preparation comparison experiments (unpublished) were undertaken previously by Yoshida and colleagues; the present work builds upon their developments.

المنارة للاستشارات
www.manaraa.com

1.2 Overview of Current Work

This section summarizes the body of work undertaken for the present thesis project. There were essentially two phases of the project: development of hardware and software tools used for bioimpedance analysis, and application of the system to investigate the impedance characteristics of the skin-electrode interface as described previously.

1.2.1 Development of Impedance Analysis System

The impedance characterization/analysis system consists of essentially four components: the stimulation/sensing hardware, the parasitic capacitance calibration/compensation software, the impedance acquisition/calculation software, and the post-hoc analysis/modeling software. Conceptual descriptions for the first three of these are detailed in the appendices and the latter in Chapter 3. Here an overview is given of the contributions made to their development during this project. Further details of the development activities are provided in Chapter 4.

As discussed in Appendix A, the stimulation/sensing hardware is a customized voltage-to-current converter with noise generation capabilities to provide a broadband stimulation current waveform. The work undertaken in this project involved creating the next generation of the hardware, including a completely redesigned PCB layout to reduce internal capacitance, migration to primarily surface-mount components for increased noise immunity, and a more stabilized design allowing for commercial fabrication.

For the parasitic capacitance calibration software, the algorithm was updated to enable completely automated calculation of the parasitic capacitance estimate (prior versions required manual bootstrapping by the user to define the region of valid data) and include iterative estimation for increased accuracy.

The impedance acquisition/calculation software is a LabVIEW-based application that uses the standard National Instruments (NI) hardware/software platform to acquire sampled waveforms of the voltage and current sense output from the impedance measurement hardware. Prior versions of the application were based on older versions of LabVIEW and

المنارة للاستشارات
www.manaraa.com

used the Traditional NI-DAQ driver API set in the backend for compatibility with legacy NI acquisition hardware. Two revisions of the application were released during the current project, one minor and one major. The minor revision updated the LabVIEW runtime environment and fixed a persistent bug causing the application to occasionally crash during data collection but continued to use Traditional NI-DAQ APIs for the acquisition backend. The major release incorporated various bugfixes and improvements to the user interface, and converted the backend to the current NI-DAQmx API set for use with newer NI acquisition hardware. The latter was a significant effort requiring several months to complete.

Finally, the MATLAB-based analysis/modeling software underwent significant updates as well. Prior versions had consisted primarily of interconnected scripts designed for manual invocation, thus requiring a substantial amount of *a priori* knowledge to use. A graphical front-end was developed to unify the set of scripts into a more intuitive and user-friendly analysis system. The interface allows the user to load any number of impedance data sets at once and view their frequency spectra before calling the Cole analysis and/or parasitic capacitance compensation routines. Among other usability improvements, it also provides the user with the option to review the results of the Cole analysis for each individual data set and choose to redo the analysis for that data set, if unsatisfactory, before saving the results. The current version of this software runs inside the standard MATLAB install environment, but could be compiled to a standalone application if desired.

1.2.2 Experimental Application of Measurement System to Skin Impedance and EMG Analysis

Experiments were conducted to determine the comparative effects of skin preparation methods on the tissue-electrode impedance and signal-to-noise ratio of surface electromyogram recordings in human subjects. A mixed set of abrasive and non-abrasive preparation methods were used on the skin prior to attachment of surface electrodes. Following preparation, full-spectrum impedance readings were taken and electromyographic activity was recorded at each preparation site. Parameter extraction using the Cole impedance model

المنارة للاستشارات
www.manaraa.com

was performed on the impedance data, and the signal-to-noise ratios of the electromyogram recordings were calculated. Statistical comparisons were examined to discover significant effects between preparation methods.

Experiments were initially performed during the summer of 2010 at the Panum Institute, the University of Copenhagen, Denmark. Additional trials were conducted during the summer of 2012 at the School of Sport and Exercise Sciences, the University of Birmingham, UK.

1.3 Organization of the Thesis

Following is a brief outline of the thesis. Background and theoretical material is presented in earlier chapters, with the experimental application following.

1.3.1 Chapter 2: Mathematical Models of Bioimpedance

In this chapter the mathematical background for impedance modeling is discussed, with special emphasis on the Cole models. Frequency-varying impedance behavior is highlighted and compared to simple linear circuit models. Similarities and differences between series and parallel versions of impedance models are discussed and quantified.

1.3.2 Chapter 3: Software Implementation and Validation of the Cole Models

This chapter describes the method developed to fit acquired impedance data to the Cole models (presented in Chapter 2) and extract all associated parameters from the model fit. The fitting/extraction algorithm is explained in detail, and experimental validation evidence is provided to demonstrate the accuracy and effectiveness of the algorithm.

المنارة للاستشارات
www.manaraa.com

1.3.3 Chapter 4: Development of the Impedance Analysis System

This chapter provides additional details on some of the specific activities associated with development of hardware and software for the impedance characterization system. High-level design diagrams, output images, and/or screenshots are included as appropriate.

1.3.4 Chapter 5: Analysis of the Effects of Skin Preparation Methods on Tissue-Electrode Interface Impedance and sEMG Recordings

This chapter details the experimental portion of the present work, covering the comparative analysis of tissue-electrode impedance in response to various types of skin surface preparation techniques as well as the companion analysis of signal-to-noise ratio in electromyographic recordings. Statistical results are discussed in detail and conclusions are evaluated.

المنارة للاستشارات
www.manaraa.com

2. MATHEMATICAL MODELS OF BIOIMPEDANCE

This chapter presents the historical development of the understanding of bioimpedance and explains the electrical and mathematical models that are used in the present work to describe the complex electric behavior of biological tissue and its parameters of interest.

2.1 Series Models

The impedance of biological tissue has long been understood to have both resistive and capacitive components. In the 1920s K.S. Cole, Hugo Fricke, and others [2–4] demonstrated that the impedance of a suspension of cells could be roughly approximated by a resistor-capacitor network similar to the one shown in Figure 2.1, whose real-imaginary plot is a perfect semicircular arc centered on the real axis. The impedance Z of such a simple RC network is given as follows:

$$Z = R_\infty + \frac{\Delta R}{1 + j\omega\tau_Z}\,, \quad \Delta R = R_0 - R_\infty\,, \quad \tau_Z = C_Z \Delta R \tag{2.1}$$

However, these early investigations also revealed a persistent deviation from linearity in many tissues: the capacitance often varies with frequency, giving rise to a depression of the circular arc in the real-imaginary impedance plot. Moreover, the capacitance depends on frequency in such a way that the phase angle of its impedance is constant (*i.e.*, frequency independent) for any given tissue [2]. The exact biophysical mechanism for this behavior is still unknown and must be described empirically [20, 21] as a so-called constant-phase element (CPE).

In 1940 Cole introduced a more complete mathematical description of tissue impedance [6], empirically describing the nonlinear behavior of the CPE in terms of the time

المنارة للاستشارات
www.manaraa.com

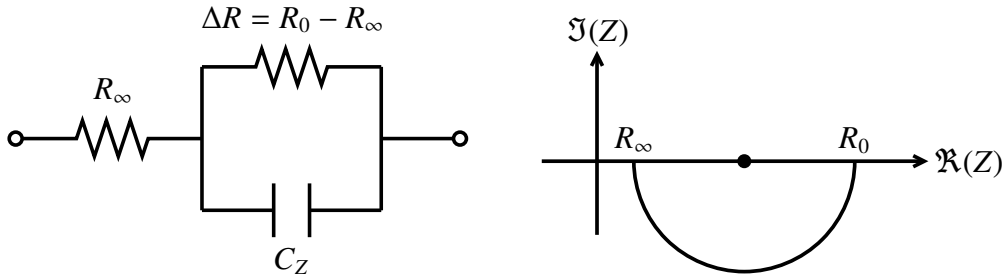

(a) Equivalent circuit diagram. The resistance symbols R_0 and R_∞ denote the resistances at zero frequency and infinite frequency respectively.

(b) Real-imaginary plot of the impedance Z for the network in (a). Note that this plot, as shown, gives no direct information about the value of the capacitance C_Z (and hence the time constant τ_Z) because the frequency parameter has been eliminated.

Figure 2.1. A simple resistor-capacitor network as a rough approximation to tissue impedance.

constant τ and a frequency exponent α. Grimnes and Martinsen [21] give the Cole equation in a useful form as follows:

$$Z = R_\infty + \frac{\Delta R}{1 + (j\omega\tau_Z)^\alpha}, \quad \Delta R = R_0 - R_\infty \tag{2.2}$$

Note the striking similarity between equations (2.1) and (2.2). The circuit description is also very similar, the capacitor being replaced by a CPE with two special properties: (1) the phase angle φ of the CPE, in accordance with Fricke's law, is directly related to the frequency exponent ($\varphi = \alpha\pi/2$), and (2) the parallel resistance ΔR actually controls the impedance magnitude of the CPE, so that the two components function together as a single "parallel Cole element" [21]. The Cole_Z circuit is shown in Figure 2.2.

Although the arc is depressed in the impedance locus of the Cole system, the circular shape of the arc is not disturbed [5]. Therefore, a circular best-fit algorithm exploiting the geometric properties of the impedance locus may be used to extract relevant Cole model parameters from impedance data.

المنارة للاستشارات
www.manaraa.com

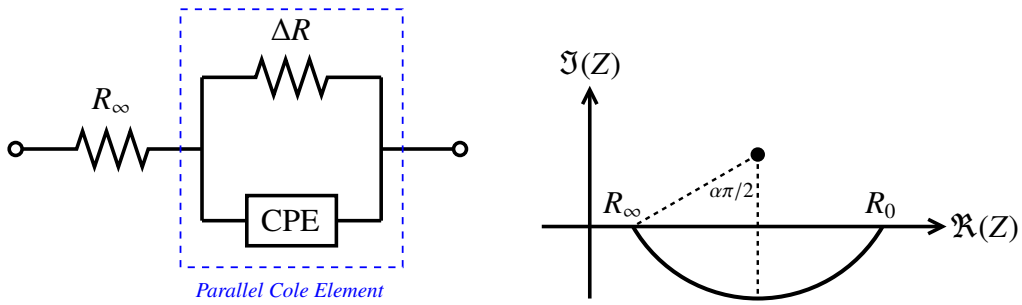

(a) Equivalent circuit diagram. This is the series version of the Cole system (the independent resistance R_∞ is in series with the Cole element).

(b) Real-imaginary plot of the impedance Z for the Cole series system in (a). As in the RC network case, the time constant cannot be determined directly from this plot.

Figure 2.2. The Cole impedance system.

2.2 Parallel Models

As an alternative to the series system representations described in section 2.1, parallel circuit models may be used instead. They exhibit the same frequency characteristics but are expressed in terms of the admittance Y instead of the impedance Z. The Cole$_Y$ equation is more convenient in situations where the corresponding parallel Cole model is more physiologically relevant than the series model [21].

The parallel equivalent of the previous RC network circuit is shown in Figure 2.3. The admittance is given as follows:

$$Y = G_0 + \frac{\Delta G}{1 + j\omega\tau_Y}, \quad \Delta G = G_\infty - G_0 = \frac{1}{R_S}, \quad \tau_Y = C_Y R_S \tag{2.3}$$

The Cole equation in admittance form is as follows [21]:

$$Y = G_0 + \frac{\Delta G}{1 + (j\omega\tau_Y)^{-\alpha}}, \quad \Delta G = G_\infty - G_0 \tag{2.4}$$

Either form of the Cole equation can be used, depending on which circuit model better describes the physiological system under investigation. The algorithm presented in this paper can be used with either the Cole$_Z$ or Cole$_Y$ models.

It is important to note that the only additional parameter introduced by the Cole model from the simple RC model is the frequency exponent α. In fact, the Cole model reduces to

المنارة للاستشارات
www.manaraa.com

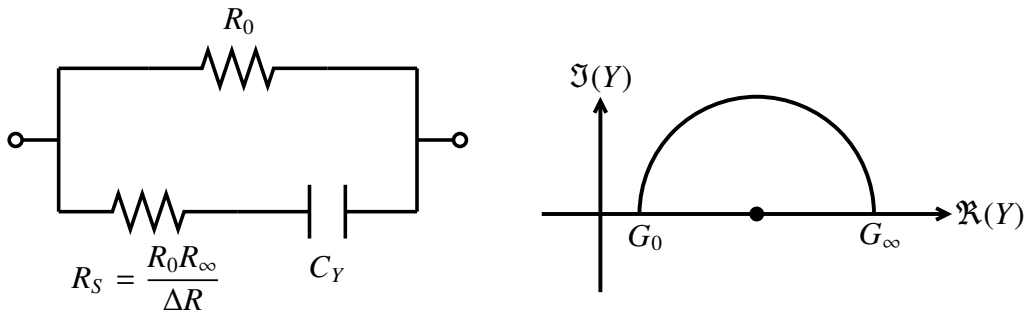

(a) Equivalent circuit diagram. Resistances are shown instead of conductances for easier comparison with Figure 2.1(a).

(b) Real-imaginary plot of the admittance Y for the network in (a). The conductance symbols G_0 and G_∞ denote the reciprocals of R_0 and R_∞ respectively.

Figure 2.3. The parallel version of the simple resistor-capacitor network.

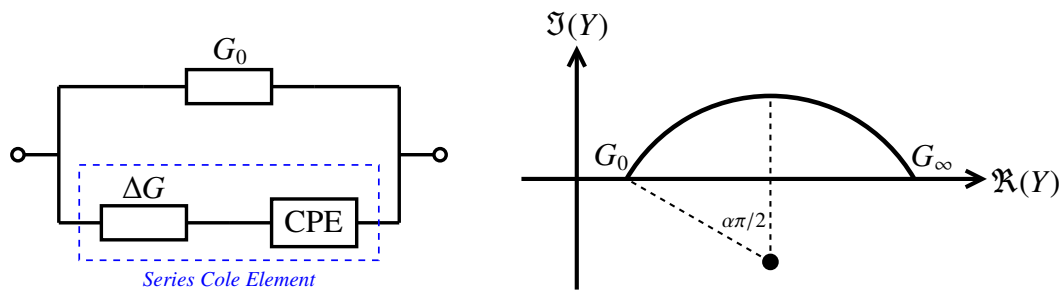

(a) Equivalent circuit diagram. This is the parallel version of the Cole system (the independent conductance G_0 is in parallel with the Cole element).

(b) Real-imaginary plot of the admittance Y for the Cole parallel system in (a).

Figure 2.4. The Cole admittance system.

the RC model in the special case $\alpha = 1$, as is evident in the model equations. This applies to both the impedance model and the admittance model, and serves as a useful benchmark to validate the algorithm used to compute impedance (or admittance), as described in Chapter 3.

المنارة للاستشارات
www.manaraa.com

2.3 Series-Parallel Relationships in the Simple Linear RC Circuit

We now return to the simple RC circuit to complete a set of mathematical relations between the series and parallel models. These will allow us to move freely from one model to the other when assessing the results of the parameter extraction process.

2.3.1 Capacitance

Since the values of both resistors can be independently deduced by frequency asymptotes, only the capacitance of the parallel circuit remains unknown. We can solve for it by equating the impedances of both circuits at all frequencies.

The real and imaginary parts of the series circuit impedance are calculated as follows:

$$\begin{aligned} Z &= R_\infty + \frac{1}{\dfrac{1}{\Delta R} + j\omega C_Z} = R_\infty + \frac{\Delta R}{1 + j\omega C_Z \Delta R} = R_\infty + \frac{\Delta R(1 - j\omega C_Z \Delta R)}{1 + (\omega C_Z \Delta R)^2} \\ &= \frac{R_\infty[1 + (\omega C_Z \Delta R)^2] + \Delta R(1 - j\omega C_Z \Delta R)}{1 + (\omega C_Z \Delta R)^2} \\ &= \left[\frac{R_0 + R_\infty(\omega C_Z \Delta R)^2}{1 + (\omega C_Z \Delta R)^2}\right] - j\left[\frac{\omega C_Z \Delta R^2}{1 + (\omega C_Z \Delta R)^2}\right] \end{aligned} \tag{2.5}$$

And for the equivalent parallel circuit, we have

$$\begin{aligned} Z &= \frac{1}{\dfrac{1}{R_0} + \dfrac{1}{\dfrac{R_0 R_\infty}{\Delta R} + \dfrac{1}{j\omega C_Y}}} = \frac{1}{\dfrac{1}{R_0} + \dfrac{j\omega C_Y \Delta R}{j\omega C_Y R_0 R_\infty + \Delta R}} = \frac{j\omega C_Y R_0 R_\infty + \Delta R}{\left(j\omega C_Y R_\infty + \dfrac{\Delta R}{R_0}\right) + j\omega C_Y \Delta R} \\ &= \frac{j\omega C_Y R_0 R_\infty + \Delta R}{\dfrac{\Delta R}{R_0} + j\omega C_Y R_0} = \frac{j\omega C_Y \dfrac{R_0^2 R_\infty}{\Delta R} + R_0}{1 + j\omega C_Y \dfrac{R_0^2}{\Delta R}} = \frac{R_0\left(j\omega C_Y \dfrac{R_0 R_\infty}{\Delta R} + 1\right)\left(1 - j\omega C_Y \dfrac{R_0^2}{\Delta R}\right)}{1 + \left(\dfrac{\omega C_Y R_0^2}{\Delta R}\right)^2} \\ &= \frac{R_0\left(1 + \dfrac{\omega^2 C_Y^2 R_0^3 R_\infty}{\Delta R^2}\right) - j\omega C_Y \dfrac{R_0^2}{\Delta R}(R_0 - R_\infty)}{1 + \left(\dfrac{\omega C_Y R_0^2}{\Delta R}\right)^2} \end{aligned}$$

المنارة للاستشارات
www.manaraa.com

$$= \left[\frac{R_0 + R_\infty \left(\frac{\omega C_Y R_0^2}{\Delta R} \right)^2}{1 + \left(\frac{\omega C_Y R_0^2}{\Delta R} \right)^2} \right] - j \left[\frac{\omega C_Y R_0^2}{1 + \left(\frac{\omega C_Y R_0^2}{\Delta R} \right)^2} \right] \tag{2.6}$$

Now, since expressions (2.5) and (2.6) are given in exactly the same form and are equivalent at all frequencies, it is possible to solve for C_Y simply by matching like terms. For example, the nonlinear frequency dependence in the denominators of both expressions must be the same, and thus we have

$$(\omega C_Z \Delta R)^2 = \left(\frac{\omega C_Y R_0^2}{\Delta R} \right)^2$$

All variables are nonnegative and so the squares may be removed. Also, the frequency may be eliminated from both sides since in the case of $\omega = 0$ the capacitances are irrelevant. Thus we arrive at the following relation between the capacitances:

$$C_Y = \left(\frac{\Delta R}{R_0} \right)^2 C_Z \tag{2.7}$$

Note that this same result would have been obtained by comparing any other pair of frequency terms, such as the numerators of the imaginary parts.

2.3.2 Time Constant

At first glance, it might seem that the time constants for the series and parallel circuits should be identical since the circuits are equivalent at all frequencies. However, the two time constants refer to different processes. The series time constant τ_Z refers to the transient voltage response to a current step input, whereas the parallel time constant τ_Y refers to the transient current response to a voltage step input. Since the circuit responds to the two types of input differently, τ_Z and τ_Y are different as well.

Although the two time constants are not the same, there is a direct relationship between them, and we can easily derive this relationship using Equation (2.7). Substituting the expressions for the time constants given in Equations (2.1) and (2.3) into (2.7), we have

$$\frac{\tau_Y}{R_S} = \left(\frac{\Delta R}{R_0} \right)^2 \frac{\tau_Z}{\Delta R}$$

المنارة للاستشارات
www.manaraa.com

and thus

$$\tau_Y = \left(\frac{\Delta R}{R_0}\right)^2 \frac{R_S}{\Delta R}\,\tau_Z = \left(\frac{\Delta R}{R_0}\right)^2 \frac{R_0 R_\infty}{\Delta R^2}\,\tau_Z$$
$$= \frac{R_\infty}{R_0}\,\tau_Z \tag{2.8}$$

This completes the equivalence relationships between the series and parallel circuit characteristics, and we restate them together as follows:

$$\Delta R = R_0 - R_\infty \qquad R_S = \frac{R_0 R_\infty}{\Delta R} \qquad C_Y = \left(\frac{\Delta R}{R_0}\right)^2 C_Z \qquad \tau_Y = \frac{R_\infty}{R_0}\,\tau_Z \tag{2.9}$$

We will use these relationships in Chapter 3 to validate the algorithm used to extract Cole parameters from data.

المنارة للاستشارات
www.manaraa.com

3. SOFTWARE IMPLEMENTATION AND VALIDATION OF THE COLE MODELS

In Chapter 2, the Cole models were presented as a mathematical description of the nonlinear electric impedance of biological tissue. In this chapter the method of software implementation for extraction of Cole parameters from data is presented, and experimental validation of the method is described.

3.1 Method

Our Cole parameter extraction algorithm employs linear algebraic and nonlinear geometric curve-fitting to select the best-fit circle for a given impedance data set. We have implemented the algorithm as an interactive, user-guided procedure in MATLAB (The MathWorks, Natick, MA, USA).

3.1.1 Input

The algorithm accepts as its input a data set consisting of paired frequency-impedance values, where the frequency values are approximately logspaced. This data set typically comes from the rapid impedance technique given in Appendix A.

3.1.2 Algorithm

1. The impedance values are corrected for the parasitic capacitance of the measurement system according to the method given in Appendix B. The user is given the option to use a default capacitance value for compensation, to compute a new value from a specified data set, or to skip compensation altogether (for pre-compensated data).

المنارة للاستشارات
www.manaraa.com

2. The corrected impedance values are converted to admittance and both are plotted in the complex plane on separate sets of axes.

3. The user is asked to choose which model to fit, impedance or admittance.

4. The data are displayed in a real-imaginary plot as before, according to the user's selection in step 3, and the user is allowed to eliminate some outlying data by zooming in to the region of interest.

5. The user is asked to choose three points on the graph that define a circle representing the user's best guess of the appropriate fit to the Cole model. This is a bootstrapping technique designed to exclude portions of the data, usually at the low-frequency end, that deviate from the circular Cole fit.

6. The circle defined by the three points selected by the user in step 5 is superimposed on the data. Any data point that lies further from the circle than a specified threshold (by default, one standard deviation) is masked from further analysis.

7. The remaining data are fitted to a circle using linear and nonlinear least-squares algorithms in tandem, and the best-fit parameters are determined.

8. Steps 6 and 7 are repeated to produce a second set of fit parameters. This time the best-fit circle from the first iteration is used in step 6 as the standard for outlier detection.

9. Both fit candidates are plotted along with the data in the complex plane, and the user is asked to indicate the better fit.

10. To avoid obtaining negative values of impedance (or admittance in Cole_Y mode), the user is given three options to choose the value of R_∞ (or G_0): the value directly computed from the circular fit, the value computed from a linear fit of the 35 highest-frequency (lowest-frequency) data points, or the value 0.1 Ω (0.1 μS).

11. Once all geometric parameters are established, they are used to estimate the time constant. The time constant is the reciprocal of the (radian) characteristic frequency,

المنارة للاستشارات
www.manaraa.com

which is the frequency at which the reactance of the circuit is maximum [21]. The geometric parameters determine the location of the point of maximum reactance, and the frequencies corresponding to the five closest data points are log-averaged to estimate the characteristic frequency, which determines the time constant.

12. The final fit candidate is superimposed on the data in a Bode plot and a real-imaginary plot, and the user is asked to indicate whether or not the fit is acceptable. If accepted, the fit parameters are stored; if not, the parameters are discarded and the algorithm returns to step 2.

3.2 Experimental Validation

We tested the algorithm with a simple RC series circuit as in Figure 2.1. The values of the three components were individually measured with a digital multimeter and are reported in Table 3.1 along with their parallel-circuit equivalents and time constants calculated using Equations (2.1), (2.3), and (2.9).

Table 3.1
RC test circuit component/characteristic values

(a) Values of actual measured components.

Symbol	Value
R_∞	9.90 kΩ
ΔR	20.06 kΩ
C_Z	0.991 μF

(b) Values theoretically calculated from component values in (a).

Symbol	Value
R_0	29.96 kΩ
R_S	14.79 kΩ
C_Y	0.444 μF
τ_Z	19.88 ms
τ_Y	6.57 ms

المنارة للاستشارات
www.manaraa.com

The complex impedance of the RC network was obtained by two-point measurement according to the method given in Appendix A. Our proposed algorithm was then employed to produce experimental values for R_0, R_∞, τ_Z, τ_Y, and α, and these values were compared to the expected values as described in the Results section.

The algorithm was also tested with commercial gel electrodes on skin tissue. Although the actual impedance of the skin and associated tissue was not independently known and thus no quantitative validation could be made against theoretical values, qualitative comparison were made against theoretical characteristics and physiologically relevant ranges of values.

3.3 Results

If our proposed algorithm is to be validated, we expect in the case of the RC network that the algorithm will calculate values for R_0, R_∞, τ_Z, and τ_Y that are nearly identical to the theoretical values in Table 3.1, and that the calculated value for α will be nearly equal to unity (indicating no depression of the circle in the real-imaginary plane, as described in Chapter 2). The actual results are reported in Table 3.2 and plotted in Figure 3.1. Comparing these results to the theoretical values, we see that all relative errors are less than 1% except for τ_Y (1.2%). The centroids of the circular fits lie on the real axis as expected. The Cole_Z and Cole_Y results also show excellent agreement with each other.

For the case of tissue-electrode impedance, we expect to obtain a circular fit with the center depressed from the real axis so that only a portion of the semicircular arc is represented; we also expect the extracted parameter values to provide at least qualitative agreement with values found in the literature. Figure 3.2 shows the plotted results and the extracted parameters. The circular arc is indeed depressed as predicted, and the extracted values for R_0 and R_∞ are in the range of those measured by Rosell *et al.* [22]. This provides qualitative validation of the parameter extraction process in a nonlinear circuit model with real electrodes.

المنارة للاستشارات
www.manaraa.com

Table 3.2
RC test circuit values calculated by Cole algorithm

Cole_Z		Cole_Y	
Symbol	Value	Symbol	Value
R_0	29.72 kΩ	R_0	29.82 kΩ
R_∞	9.86 kΩ	R_∞	9.86 kΩ
τ_Z	19.98 ms	τ_Y	6.65 ms
α	0.999	α	1.000

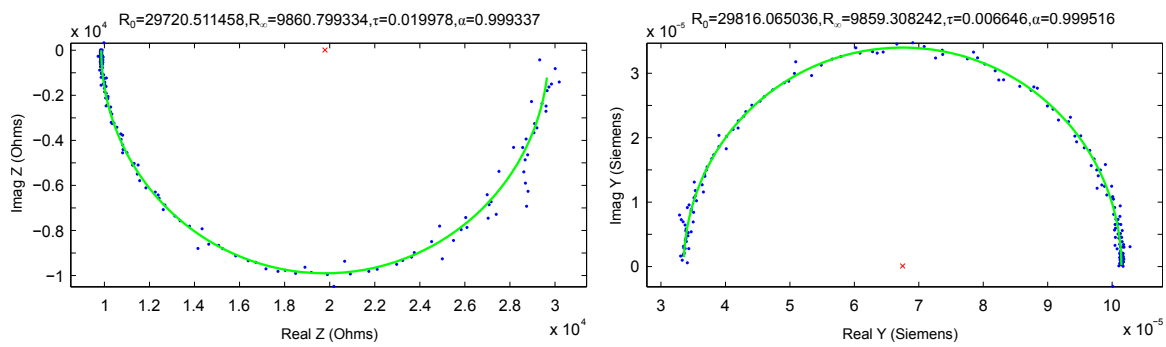

Figure 3.1. RC circuit impedance data fitted to the Cole_Z (left) and Cole_Y (right) circuit models. Acquired data are shown in blue with the fitted curve in green, and the centroid is marked in red. Parameter values extracted from the fit are shown at the top of each graph.

3.4 Discussion and Conclusions

Exploitation of the geometric properties of the Cole models in the complex plane results in a simple yet powerful technique for *in vivo* impedance analysis. Both the impedance and the admittance models may be tested simultaneously for a given data set and the better fit chosen by inspection. Computation involves straightforward linear algebraic and iterative techniques that can be easily implemented in a mathematical data processing software

المنارة للاستشارات
www.manaraa.com

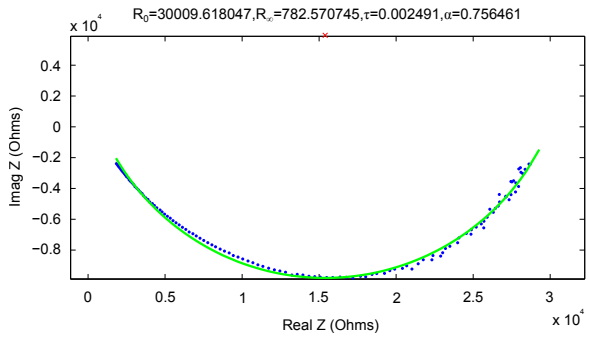

Figure 3.2. Tissue-electrode impedance data fitted to the Cole_Z circuit model. The centroid (marked in red at the top of the plot window) is located beyond the real axis with respect to the data, as predicted by the model.

package such as MATLAB. Additionally, the interactive nature of our implementation allows the user to view the analysis in progress and guide the algorithm to the most relevant portions of the data. The result is a concise set of parameters that can be used to quantitatively assess a variety of physiological characteristics of a particular type or sample of tissue. In Chapter 5, the algorithm is used for comparative assessment of skin impedance under a variety of preparation methods.

المنارة للاستشارات
www.manaraa.com

4. DEVELOPMENT OF THE IMPEDANCE ANALYSIS SYSTEM

As outlined in the introduction, a substantial amount of development in support of the complex impedance analysis process was required as a supporting aim to the project. Prototypes and preliminary versions of the different system components were provided at the outset, and the goal of the additional development was primarily to stabilize, update, and improve these preliminary components into a more mature set of research tools to support the work of our primary research aim and similar endeavors.

Of the four system components outlined in the introduction, all are covered at least briefly from a theoretical perspective in other chapters or in the appendices. The intent of this chapter is to provide further elaboration on the technical aspects of the components and their development. Because the Cole parametrization and parasitic capacitance calibration/compensation algorithm implementations have already received sufficient treatment in Chapter 3 and Appendix B respectively, they will not be covered in detail here; instead the focus will be on the method of integration of these two algorithms into a unified system behind a front-end graphical user interface (GUI).

4.1 Stimulation/Sensing Hardware

The stimulation/sensing hardware is responsible for creating the broadband noise signal used for spectral impedance characterization, passing the noise signal to the electrode contacts in either a voltage-source waveform or an equivalent current-source waveform, measuring both the voltage across the electrodes and the current passed through the electrodes, and providing final amplification of the voltage and current waveforms to be subsequently acquired by an external recording system. A functional block diagram is given in Figure 4.1.

المنارة للاستشارات
www.manaraa.com

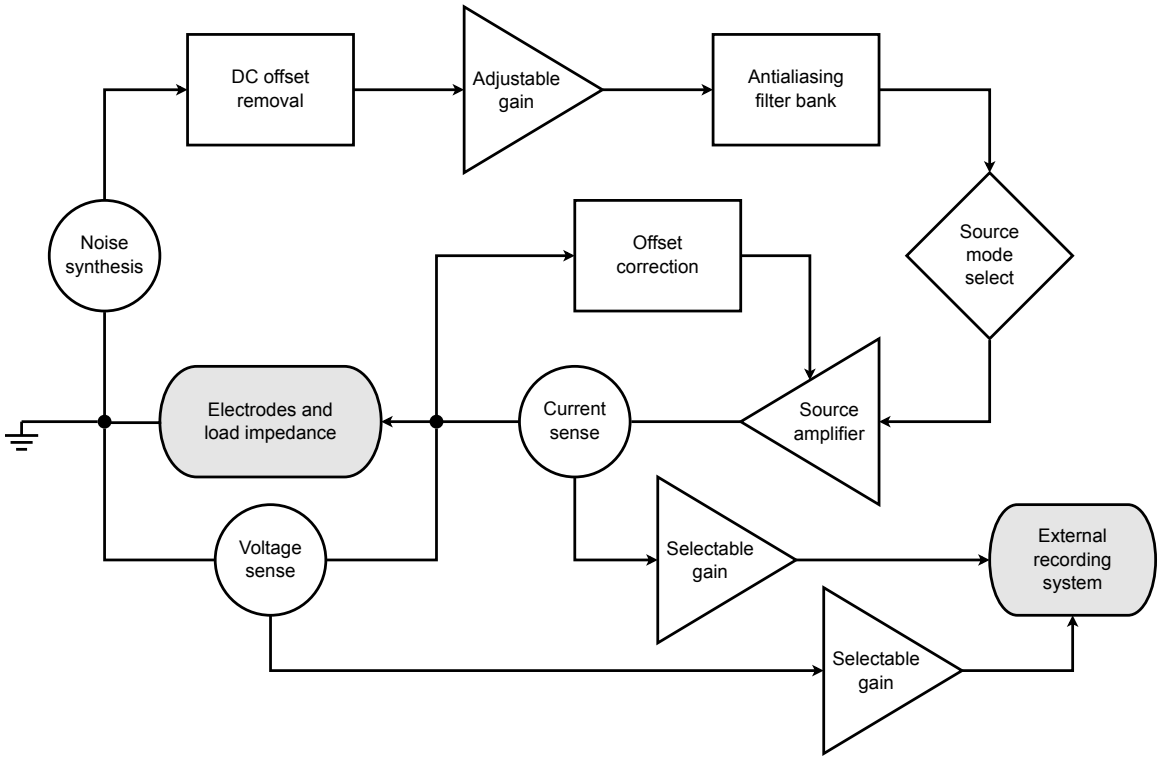

Figure 4.1. Functional pseudo-circuit block diagram of the noise stimulation/sensing circuit. Shaded blocks indicate components not integrated into the hardware design but connected via the integrated BNC jacks.

The prior revision of this measurement hardware was functional but not fully integrated. The noise synthesizer and its offset removal and gain stages were housed in a separate unit, contained their own battery power supply, and had to be connected via cable to the driving/sensing circuit. We determined that it was not desirable to maintain the two subcircuits in separate units, but rather to have all parts of the design as closely integrated as possible. We combined the two subcircuits in one PCB layout with shared onboard power regulation, connected to an external battery power supply by means of a cable and plug.

All stages of the hardware circuit design were carried out using the open-source gEDA software suite. This included reproducing the schematic capture drawings as part of migration from an obsolete proprietary software package. Following the updates to the schematics, the PCB layout was completely redesigned. This was a complicated task due to a few

المنارة للاستشارات
www.manaraa.com

conflicting interests: we wanted to (1) keep the form factor reasonably small and easily portable, (2) keep the driving and measurement stages away from each other to minimize noise contamination, and (3) include the entire circuit on a single two-layer board, including power regulation, noise generation and conditioning, current/voltage source manipulation, offset compensation, output sensing and amplification, and BNC connectors for all electrode and sensor outputs. In addition, reducing the internal capacitance of the circuit was an important consideration, as was maintaining very low impedance between the external signal connectors and the board. We used large traces to reduce path impedance and noise coupling, ground planes on both sides of the board to suppress environmental noise, wide trace clearance to minimize capacitance to the ground plane, and op-amp guard rings to reduce leakage currents [23].

The final design fit on a two-sided PCB (approximately 5×4 in). After commercial fabrication, the PCB was manually populated and mounted in a box (shown in Figure 4.2 along with images of the schematic and PCB layout designs). The new design was shown to result in nearly 50% less internal capacitance compared to the previous implementation, as shown in Figure 4.3.

4.2 Impedance Acquisition/Calculation Software

The purpose of this software is to manage the multichannel acquisition required to pseudo-simultaneously record the voltage and current waveforms from the stimulation/sensing box. It allows the user to specify the recording configuration used in the hardware (2-, 3-, or 4-point), the sweep duration, and other acquisition settings. After acquisition, the software calculates the impedance using an empirical transfer function as described in Appendix A, and the user is allowed to view the impedance plots as a function of frequency or in the complex plane. The user can also add comments for each sweep before saving the results and lists of settings to ASCII text files. Additional output files (optional) include the impedance data saved in MATLAB-compatible data format and/or the raw acquired voltage and current waveforms, also in MATLAB format.

المنارة للاستشارات
www.manaraa.com

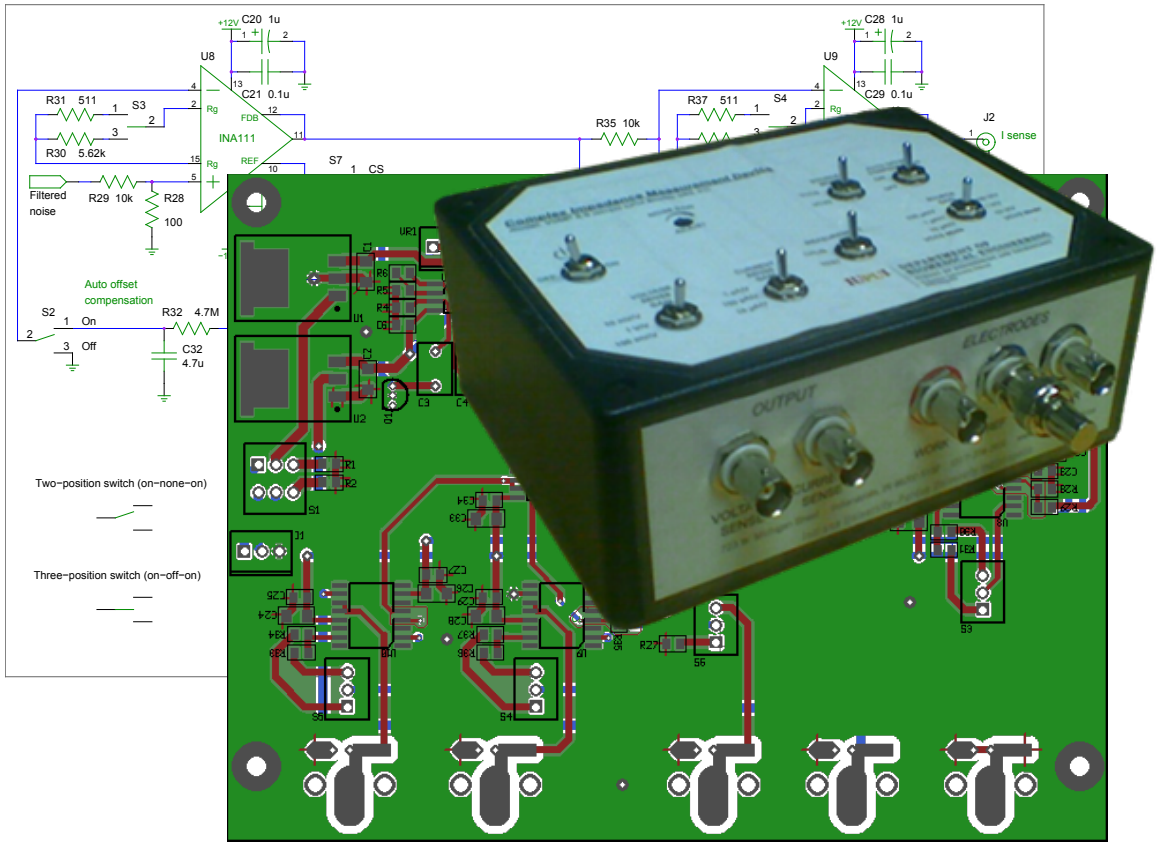

Figure 4.2. Design process view of the stimulation/sensing hardware, including circuit schematic, PCB layout, and photo of completed product.

The software also includes a built-in virtual oscilloscope for convenient viewing of the signal prior to acquisition. The oscilloscope can be turned on and off as desired, and automatically pauses when recording is initiated.

The first development task with regard to this software was to update the codebase to LabVIEW 8.6 which was our main development environment, and to fix a persistent bug that caused the program to occasionally crash during signal acquisition. The fix involved repairing an incomplete semaphore implementation that allowed two routines to attempt to access identical hardware resources at the same time. Upon completion of these tasks, the software was released as version 0.8, continuing to use the Traditional NI-DAQ driver backend for compatibility with legacy NI acquisition hardware.

المنارة للاستشارات
www.manaraa.com

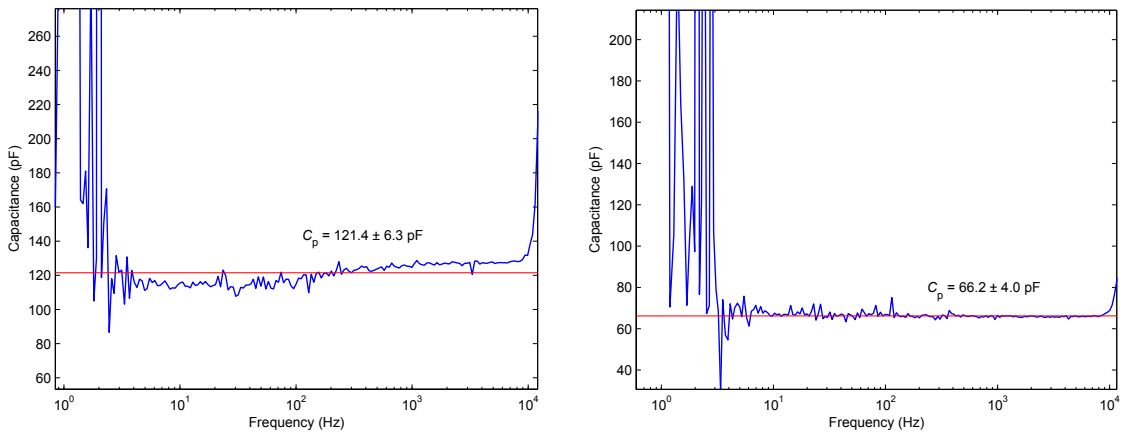

(a) Previous revision.

(b) Current revision.

Figure 4.3. Comparison of estimates of parasitic capacitance in the measurement apparatus using the previous and updated hardware revisions.

The second and much larger task in preparation for the next release (version 1.0) was to migrate the acquisition system to the newer NI-DAQmx driver backend. All functions interfacing with the hardware had to be converted to their equivalent functions in the new API. Although many of the functions operate in the same way and could be seamless substituted into the existing codebase, and help topics and conversion sheets have been made available by National Instruments, some aspects of the system operate differently and required more involved code changes for functional equivalence. (For example, the DAQmx API relies heavily on a revised property scheme in which hardware settings and properties are accessed and set individually through so-called "property nodes" in LabVIEW rather than through function calls.) The oscilloscope and the recording module also used separate acquisition routines, so it was necessary to convert both. The oscilloscope module included a high-level wrapper function to generate an analog waveform, for which there was, oddly enough, no equivalent in DAQmx. We were thus forced to generate an equivalent wrapper from scratch in order to continue the previous behavior.

In addition to the driver platform migration, several other fixes and usability improvements were included in the release. On program launch, if a hardware device corresponding to the default device ID is not found, the software will query all devices connected to the

المنارة للاستشارات
www.manaraa.com

PC and allow the user to choose which to use for acquisition. General window behavior was also improved, in particular the close functionality which was not well integrated into the program flow and in some cases caused the program to hang. An option was also added to allow the user to show/hide the oscilloscope as desired during operation. Adjustments were made to significantly reduce CPU usage with minimal loss of execution speed. A screenshot of the released software with a portion of the code in view is provided in Figure 4.4.

Figure 4.4. Screenshot of cImp 1.0, the updated release of the acquisition/calculation software. The virtual oscilloscope is shown together with the main window and the recording popup, with a view of the code in the background.

المنارة للاستشارات
www.manaraa.com

4.3 Post-Hoc Impedance Data Processing Software

The focus for improving the impedance characterization software was on unifying the existing MATLAB routines behind a simple, user-friendly graphical user interface (GUI). The application, cImpAnalysis, consists of a window with a set of axes to display impedance data sets as magnitude and phase versus frequency along with a set of user controls (see Figure 4.5).

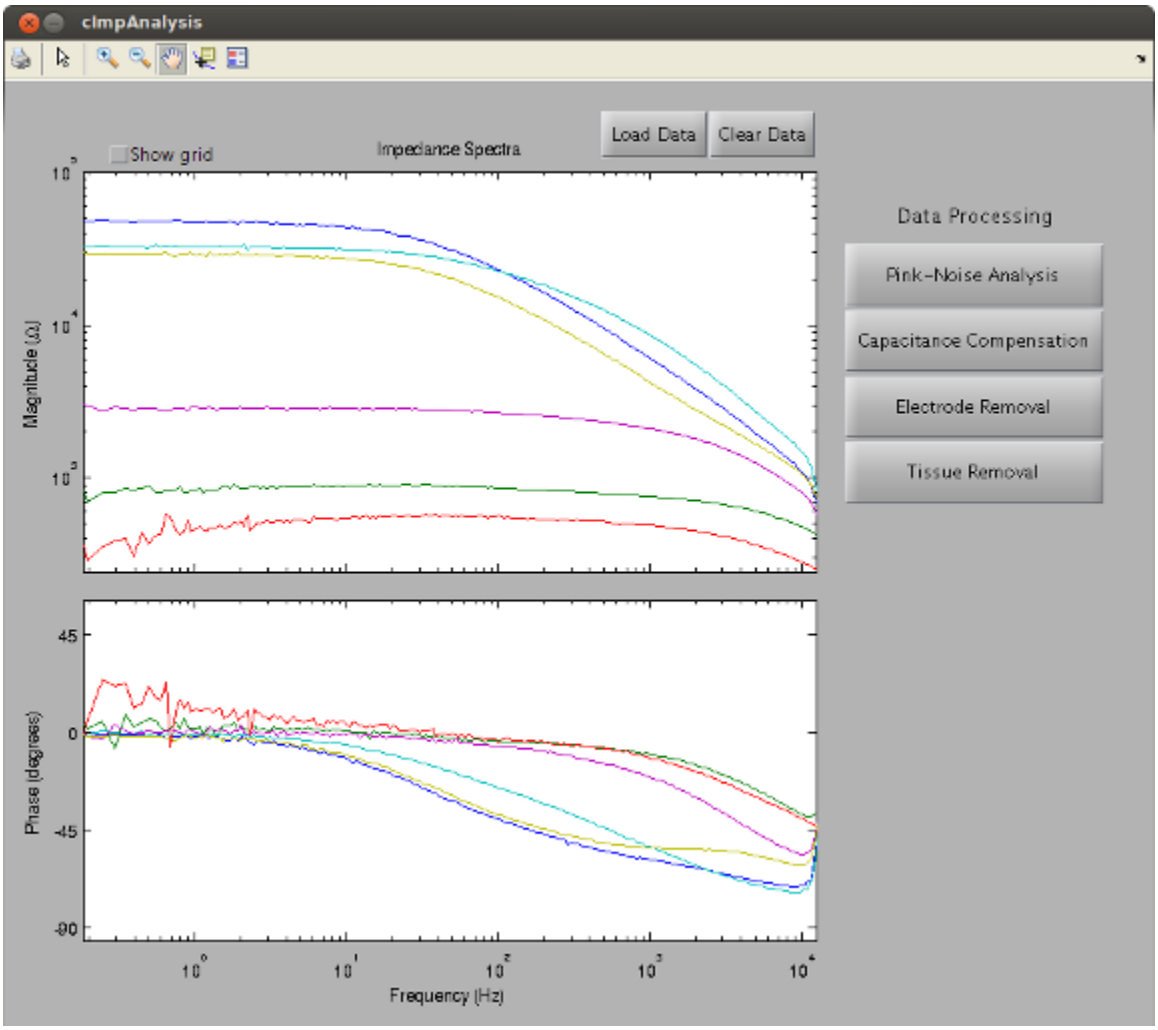

Figure 4.5. Screenshot of cImpAnalysis. An example data set has been loaded into the plot area.

المنارة للاستشارات
www.manaraa.com

The user begins by loading one or more data sets into the plot area using standard file selection dialogs. Error checking is included to warn the user if an invalid file is loaded. Several of the standard MATLAB plot editing functions are provided for convenience although they do not affect subsequent analysis. The plot area can be cleared and/or new data sets loaded as desired with the Load Data and Clear Data buttons. Once the user has loaded all data sets he intends to analyze, several analysis functions are available to run on the displayed data.

The Pink-Noise Analysis button calls the Cole analysis routine described in Chapter 3; the Capacitance Compensation button calls the parasitic capacitance correction routine described in Appendix B, then applies the compensation to the displayed data and saves the corrected impedance data in a directory of the user's choice.

The Electrode Removal and Tissue Removal buttons were newly developed and are somewhat more specific to the particular experiments discussed in Chapter 5; they compensate data for the internal impedance of the electrodes and the impedance of deeper tissue between the electrodes (see Figure 5.2 for details). Unlike the other routines, electrode removal operates directory-wise (*i.e.*, it attempts to find and correct all uncompensated data sets in a specified directory instead of operating on the data displayed in the plot area). Both electrode removal and tissue removal operate on data non-destructively: rather than modify the original data, they prompt the user for a directory in which to save the compensated data. Electrode impedance is measured by shorting the electrodes together and obtaining the impedance spectra as for normal loads; deep-tissue impedance is obtained by designating a data set in which most of the skin impedance has been removed and calculating R_∞ via Cole model analysis.

Although the primary goal for this phase of software development was to provide a simple entry point for the user to access the Cole parameter extraction and capacitance compensation methods, a few improvements were made to the processing routines themselves. In addition to the new development of the electrode and deep-tissue compensation scripts, a bug in the Cole analysis routine was fixed that had incorrectly handled the user's best-guess fit of the circle when applying outlier masking. Additionally, a feature was

المنارة للاستشارات
www.manaraa.com

added to allow the user to redo the Cole analysis an indefinite number of times for a particular data set if the fit was unsatisfactory. Finally, the parasitic capacitance estimation algorithm had originally required manual bootstrapping to select the relevant portion of data due to the quantity of outliers and the difficulty of determining the stable region of data. To offset this difficulty, the algorithm was updated to begin by searching for phase values near $-90°$, which automatically eliminates most outliers and allows the the rest to be eliminated by threshold testing.

4.4 Summary

The development activities described in this chapter were intended to build on previous work and achieve a well-integrated and user-friendly impedance measurement system. While additional improvements could certainly be made to the system — for example, cImp could allow the user to specify hardware configuration defaults in a configuration file, and cImpAnalysis could provide more flexible means to identify types of impedance files at interim stages of analysis — overall the system is greatly improved and able to efficiently handle collection and analysis of impedance data in a straightforward setup. The measurement hardware features greatly reduced internal capacitance as noted previously, and the physical design is more robust, repeatable, and self-contained. On the software side, cImp now supports the updated driver set used in newer NI hardware, runs more efficiently, and is more user-friendly. cImpAnalysis allows the user to view data before analyzing and provides easy access to the necessary routines. Overall the system is significantly better equipped for future investigational efforts, and certainly fulfills the auxiliary aim for the present work.

المنارة للاستشارات
www.manaraa.com

5. ANALYSIS OF THE EFFECTS OF SKIN PREPARATION METHODS ON TISSUE-ELECTRODE INTERFACE IMPEDANCE AND SEMG RECORDINGS

5.1 Introduction

The preceding chapters provided the theoretical background for analysis of bioimpedance and the algorithm used for implementation. This chapter describes the use of Cole model analysis to investigate and quantitatively compare the effects of different methods of skin preparation on the impedance of the tissue-electrode interface in humans. The signal-to-noise ratio (SNR) of surface electromyogram (sEMG) activity was also examined for each type of skin preparation and compared with the corresponding impedance results.

A few of the most common methods of skin preparation prior to placement of surface electrodes are shaving, abrasion and cleaning with alcohol. These and other similar methods were reviewed by the European concerted action SENIAM as to their relative frequency of use (as reported in the literature) for electromyographic recordings [13]; however, to our knowledge the efficacy of such procedures has never been systematically and quantitatively compared. Accordingly, the objective of the experiments described in this chapter was to determine which of these preparations, if any, had a significant effect on the tissue-electrode impedance and/or the SNR of sEMG recordings, and thus to provide a quantitative validation of recommended procedures for skin preparation.

المنارة للاستشارات
www.manaraa.com

5.2 Methods

5.2.1 Participants

Fourteen volunteer participants, eleven males and three females, were included in the experiments. Some participants were tested multiple times, resulting in a total of 23 trials. Mean age (counting all 23 data sets) was 29.5 ± 8.6 yr. The experiments were performed in accordance with the Declaration of Helsinki and informed written consent was obtained for all participants. The study was approved at the University of Copenhagen, Denmark by the Videnskabsetiske Komité for Københavns og Frederiksberg Kommuner and at the University of Birmingham, UK by the University of Birmingham Science, Technology, Engineering and Mathematics Ethical Review Committee.

The impedance data for two of the trials were unable to be collected due to equipment malfunction; thus the impedance analysis is based on the remaining 21 data sets, while the sEMG analysis includes all 23 sets.

5.2.2 Skin Preparation

Six different methods of skin preparation were tested on an area of skin located on the ventral surface of the thigh, over the quadriceps muscle group. The area of skin was divided into a grid consisting of six cells in a 3×2 arrangement, each cell receiving one of the set of preparations. A list of the different preparation methods, along with the abbreviation codes used in the analysis, is given in Table 5.1. Following preparation, a pair of adhesive Ag/AgCl gel electrodes (N-10-A, Ambu A/S, Ballerup, Denmark) was attached to each patch of skin with an inter-electrode distance of approximately 25 mm. A photo of a typical electrode arrangement is shown in Figure 5.1. A lead plate in a moistened cloth sleeve, placed immediately proximal to the knee, was used as a grounding electrode for the sEMG measurements.

المنارة للاستشارات
www.manaraa.com

Table 5.1
Skin preparation methods

#	*Preparation method*	*Abbreviation*	*Description*
1	No preparation	NP	Used as negative control.
2	Hair removal	HR	Non-abrasive hair removal using electric hair clippers. Care was taken to minimize skin contact that might result in abrasion.
3	Shaving	Sh	Common shaving technique using manual hand razors. Unlike Preparation 2, no attempt was made to avoid or minimize the abrasive action of the razor blade.
4	Abrasion	Abr	Preparation 2 followed by surface abrasion with medical-grade sandpaper using medium-light pressure for 10–15 s.
5	Alcohol	EtOH	Preparation 2 followed by cleaning with medical alcohol wipe.
6	Abrasion + alcohol	Abr+EtOH	Preparation 4 followed by alcohol wipe as in Preparation 5.

5.2.3 Spectral Characterization of Tissue-Electrode Interfacial Impedance

The complex impedance between each pair of electrodes was obtained by two-point measurement according to the method given in Appendix A. The open-circuit and short-circuit impedances between the electrodes were also recorded, the former to account for the parasitic capacitance of the cables and the latter to account for the internal impedance of the electrodes. Compensation for these two circuit elements leaves the impedance of the two tissue-electrode interfaces plus the deeper tissue between the electrodes. The deep-tissue impedance — which is assumed to be primarily resistive, approximately corresponding to R_∞ in the Cole$_Z$ model (Figure 2.2) — is subtracted out, leaving (twice) the impedance of

المنارة للاستشارات
www.manaraa.com

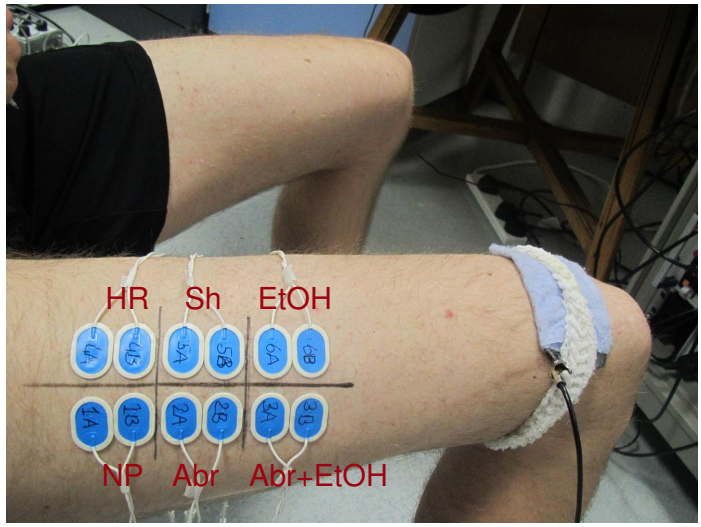

Figure 5.1. Typical arrangement of electrode pairs on patches of skin. Labels added for clarity.

the tissue-electrode interface (more correctly, the complex sum of the two tissue-electrode impedances since they are in series and cannot be discriminated by two-point measurement). This process is illustrated schematically in Figure 5.2.

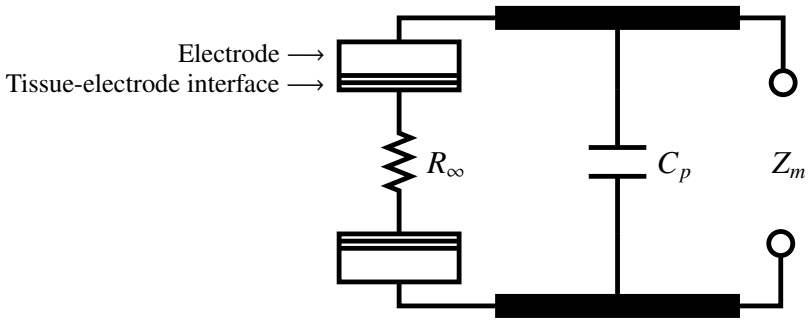

Figure 5.2. Schematic breakdown of measured impedance Z_m. In order to obtain the impedance of the tissue-electrode interface, Z_m must be compensated for (1) the parasitic capacitance C_p of the lead cables through the air, (2) the internal impedance of both electrodes, and (3) the resistance of deeper tissue between the electrodes, assumed equal to R_∞ [24].

The interfacial impedance was then analyzed using the Cole parameter extraction algorithm (Chapter 3) and compared across preparation methods using the low-frequency

المنارة للاستشارات
www.manaraa.com

asymptote R_0 as a quantitative measure. (Again it should be noted that the computed values for R_0 will be nominally twice the actual values due to both electrode impedances being modeled together as a lump sum. For statistical comparison this is not a problem since all impedance measurements were analyzed in the same way.) The analysis was run as a two-way ANOVA with preparations and data sets as factors. In order to satisfy the statistical assumptions for a valid ANOVA, namely normality and homoscedasticity in the residuals, it was necessary to scale R_0 by a power transform [25]; thus R_0^k where $k = 0.0565$ is actually the measure of impedance used in the ANOVA.

5.2.4 SNR Validation Using sEMG

In addition to the impedance measurements, sEMG was also obtained at rest and at maximum voluntary contraction (MVC) from each pair of electrodes. For the MVC recordings, the participant was placed in a sitting position with the knee at or near a right angle. The lower leg was constrained and the participant was instructed to maximally contract the quadriceps muscles by attempting to extend the leg. The sEMG signals were band-pass filtered (10 Hz–1 kHz) and sampled at 5 kHz for 5 s through a 12-bit A/D board (NI DAQCard-6062E, National Instruments, Austin, TX, USA) using custom LabVIEW-based acquisition software.

Quiescent recordings were used as the baseline noise level for calculating the signal-to-noise power ratio. Background noise was assumed to be uncorrelated with the sEMG, thus allowing the signal power and noise power in the sEMG recordings to be separated and the SNR calculated as follows (where s is the desired sEMG signal, n is the noise, and var( ) represents sample variance):

$$\frac{\mathrm{var}(s+n)}{\mathrm{var}(n)} = \frac{\mathrm{var}(s)+\mathrm{var}(n)}{\mathrm{var}(n)} = \frac{\mathrm{var}(s)}{\mathrm{var}(n)} + 1 = \mathrm{SNR} + 1$$
$$\Rightarrow \mathrm{SNR} = \frac{\mathrm{var}(s+n)}{\mathrm{var}(n)} - 1 \tag{5.1}$$

For the quiescent recordings, var(n) was calculated from the entire 5-second sweep. For the MVC recordings, due to substantial variation between data sets in the duration of the

المنارة للاستشارات
www.manaraa.com

muscle contraction, only ~1 s was used for the calculation of var($s + n$) so that the duration of signal analyzed would be uniform across all data sets. Once calculated, the SNR was then compared across preparation methods in a two-way ANOVA with preparations and data sets as factors, similar to the impedance analysis. Likewise, the SNR also required a power transform ($k = 0.1565$) to satisfy the normality and homoscedasticity assumptions for the ANOVA.

5.2.5 Noise Immunity Test

Whereas the SNR test was intended to validate the overall noise performance of the tissue-electrode system with respect to both internal and external background noise, we also wanted to evaluate the sensitivity of the system to specific, induced environmental noise. This was done by placing a line-powered (50 Hz) incandescent light bulb at a distance of 2 m from the electrodes and recording the quiescent surface potential for 10 s, plugging in the light at approximately the halfway point. (This test was not performed on all participants as it was not the primary objective of the study; however, we did obtain a substantial number of data sets, twelve in all.) In some of the recordings, small intermittent bursts of muscle contraction were provided for enhanced visual contrast. For all recordings, the peak-to-peak amplitude of the surface potential with the light on was measured. Statistical comparison across preparations and data sets was performed in the same way as for the other recordings. The power transform required to satisfy the ANOVA actually turned out to be negative for this test ($k = -0.2268$). This means that the quantity being statistically compared is really the (scaled) reciprocal of the peak-to-peak noise amplitude, which may be interpreted as the degree of noise immunity in the tissue-electrode system.

5.3 Results

A typical example of the complex impedance spectra measured for each preparation along with the raw sEMG signals recorded at MVC are shown in Figure 5.3. Correspondingly, the aggregate statistical results of the impedance and SNR tests across preparations

المنارة للاستشارات
www.manaraa.com

are depicted in Figure 5.4. Non-abrasive preparation types are shown on the left side of each statistical plot and abrasive preparations on the right. Thus it is immediately apparent that abrasive preparations result in a lower tissue-electrode interfacial impedance and higher SNR. Similarly, the results of the noise immunity test are plotted in Figure 5.5, and here it is evident that abrasive preparations result in increased immunity to the induced noise. Any pair of data points that differ by a greater margin than the distance indicated by the arrows on the graphs, are statistically significant. Following are more detailed results from each analysis test.

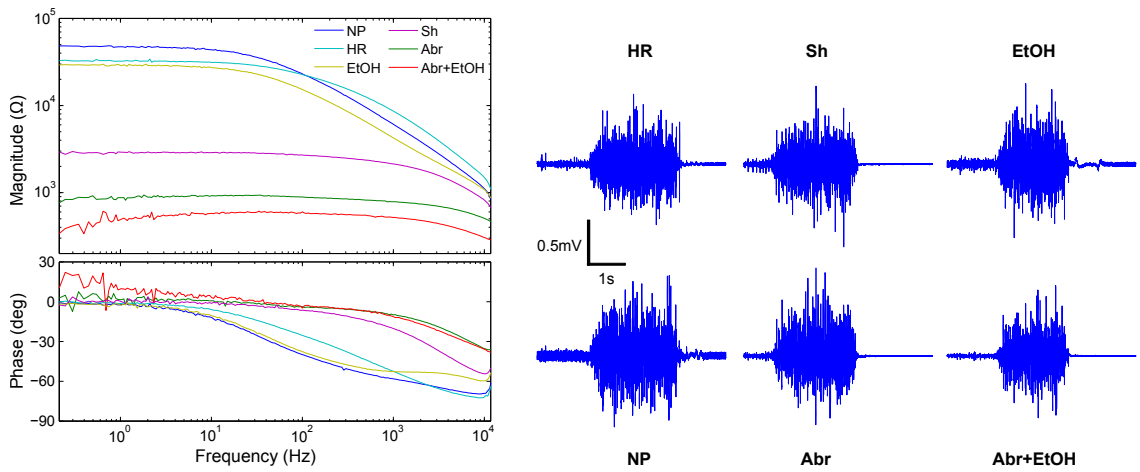

(a) Typical example of complex impedance spectra for the tissue-electrode interface.

(b) Typical example of sEMG recordings at MVC. The two signals in each column were recorded simultaneously.

Figure 5.3. An example data set with impedance and sEMG recordings.

5.3.1 Impedance Tests

Interactions between preparations and data sets were significant at the 0.05 level. However, since the interactions were not significant at the 0.01 level and the p-values for the main effects were substantially smaller than for the interaction, a reduced (non-interaction) model was considered adequate. Under the reduced model, both preparations and data sets were found to be significant ($p \ll 0.001$). Post-hoc pairwise comparisons among preparations using Tukey's honestly significant difference (HSD) test and Fisher's least significant

المنارة للاستشارات
www.manaraa.com

difference (LSD) test resulted in complete bifurcation of the preparations into two groups: Preparations {1, 2, 5} and {3, 4, 6} (as numbered in Table 5.1). Within these two groups, no two preparations were significantly different at the 0.05 level, whereas all pairwise comparisons across groups were significant.

5.3.2 SNR Tests

Interactions between preparations and data sets were nonsignificant at the 0.05 level. Using a reduced (non-interaction) model, both preparations and data sets were found to be significant ($p \ll 0.001$). Post-hoc pairwise comparisons among preparations were made using the Tukey HSD and Fisher LSD tests as for the impedance data. (The two tests showed minor differences in their groupings, and in such cases the Fisher LSD test was preferred since it more clearly resolves pairwise differences when the overall model is shown to be significant [25].) The resultant groupings are nearly identical to those in the impedance tests, except that Preparation 3 (razor shave) features a SNR that is less than the sandpaper preps ($p = 0.014$) but larger than the non-abrasive preps ($p = 0.007$).

5.3.3 Noise Immunity Tests

Interactions between preparations and data sets were nonsignificant at the 0.05 level. Using a reduced (non-interaction) model, both preparations ($p \ll 0.001$) and data sets ($p = 0.001$) were found to be significant. Post-hoc pairwise comparisons among preparations were made using the Tukey HSD and Fisher LSD tests as for the impedance data, and the resultant groupings are identical.

5.4 Discussion

Across preparation methods, the trend in sEMG signal-to-noise ratio is essentially the inverse of the trend in the impedance of the tissue-electrode interface, as shown in Figure 5.4. This strongly suggests that the interfacial impedance is a major contributor to

المنارة للاستشارات
www.manaraa.com

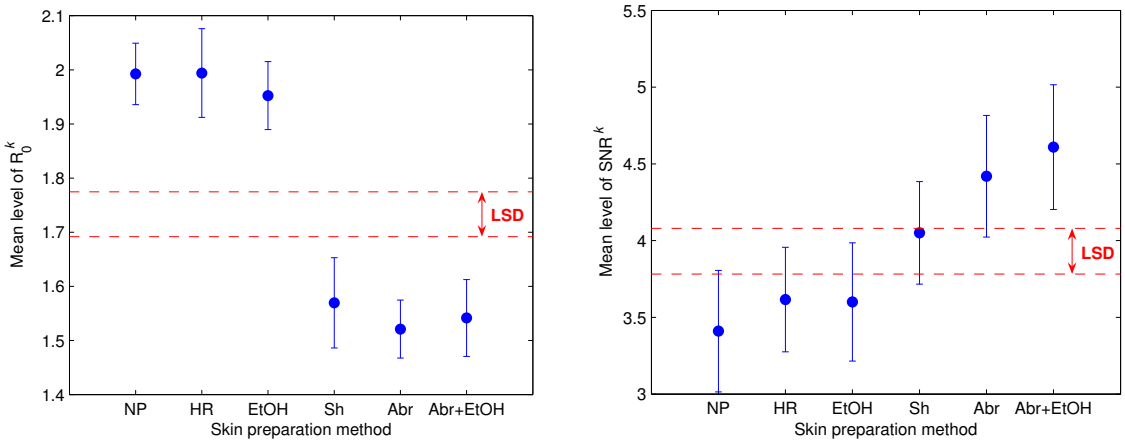

(a) Mean values of impedance, power-scaled (k = 0.0565) for homoscedasticity. Number of data sets n = 21.

(b) Mean values of scaled SNR at MVC, power-scaled (k = 0.1565) for homoscedasticity. Number of data sets n = 23.

Figure 5.4. Aggregate mean results over all data sets for each preparation type. Error bars represent 95% confidence intervals. The Fisher LSD for pairwise means comparisons among preparation types is shown in red. These results demonstrate that abrasive preparations correlate to lower impedance and higher SNR.

noise in sEMG recordings. Moreover, the Tukey and Fisher LSD groupings for impedance and SNR are nearly identical. Referring to Table 5.1, the primary difference between these two groups (Preparations {1, 2, 5} and {3, 4, 6}) is clearly the degree of abrasive action involved in the preparation. In the first group, little or no abrasion is involved in any preparation; in the second group, all preparations involve some degree of abrasion, with either sandpaper or a hand razor. It is therefore likely that the uppermost layer of the skin, the stratum corneum, is responsible for the majority of the impedance barrier, and that abrasion is effective in removing the stratum corneum to such an extent as to significantly reduce the impedance and increase the signal-to-noise ratio.

The recordings from razor-shaved skin featured a SNR that was significantly different than either the sandpaper preps or the non-abrasive preps, essentially forming a "middle ground" between the two main groups. Given that the level of abrasive action in this prep would likewise be in between the other prep types, this result makes sense and supports

المنارة للاستشارات
www.manaraa.com

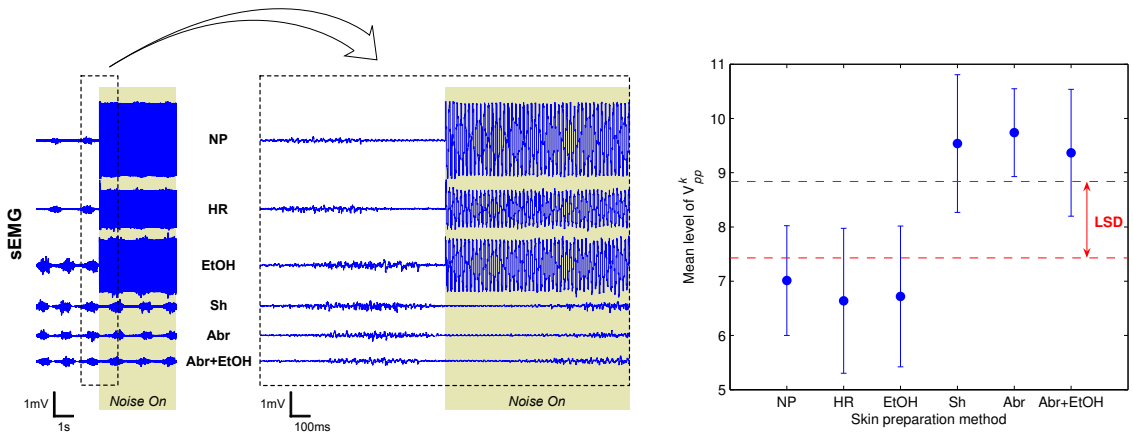

(a) Example recording with induced 50-Hz noise. Signals were recorded in three 10-second sweeps, two channels at a time. The time-expanded view to the right shows the periodic nature of the noise.

(b) Mean values of scaled noise immunity. As noted previously, the noise immunity was calculated from the peak-peak noise voltage V_{pp} by a power transform V_{pp}^k where $k = -0.2268$ (necessary for homoscedasticity as in the other analyses). Number of trials $n = 12$.

Figure 5.5. Raw recording example and aggregate mean results for the noise immunity tests. These demonstrate both graphically and statistically that abrasive preparations correlate to substantially increased immunity to induced noise.

the proposition that abrasion increases signal quality. The question remains why there was no corresponding "middle ground" in the impedance of the razor-shaved skin (*i.e.*, no significant difference from the sandpaper preps). There is a slight trend toward higher impedance in the razor shave, but the difference is not significant. This point should be further investigated with a larger sample size to determine if significant differences might exist, or if the relationship between impedance and SNR is of a more complex nature.

It is also interesting to note that application of alcohol, despite its longstanding popularity as a method for skin preparation, does not significantly affect the interfacial impedance or the SNR. As can be seen in Figure 5.4, there are slight differences between similar preps with and without alcohol, but no statistical significance and not even a consistent trend. These results are consistent with the work of Hanish *et al.* who showed that alcohol was not effective in suppression of motion artifacts in ECG recordings during exercise [9]. Thus

المنارة للاستشارات
www.manaraa.com

it is apparent that alcohol is not effective in reducing contact impedance or improving signal clarity.

Finally, no significant difference in impedance or SNR was found between non-abrasive hair removal and the negative control, indicating that the presence or absence of hair probably does not substantially affect the integrity of the tissue-electrode interface. However, there is a slight trend toward increased SNR with hair removal, and thus further investigation may be warranted to examine the possibility of a significant effect.

We thus conclude that abrasion is the key to obtaining a low interfacial impedance and high SNR. This is probably best explained in terms of impedance balance and common-mode rejection: a lack of abrasion leads to a higher impedance across the electrodes as well as a difference between the two tissue-electrode interface. This allows more noise to appear across the electrodes as a differential-mode signal rather than common-mode. Once the noise is present as a differential-mode signal, it will inevitably (and indeed necessarily) be captured in the recording even by excellent recording hardware with otherwise high common-mode rejection characteristics [18]. Thus, in order to ensure accuracy and stability in recorded biopotentials, it is essential to provide a sufficient degree of abrasion to compromise or remove the high-impedance layer of skin and preserve the noise rejection characteristics of the recording circuit.

A limitation of our analysis is the fact that we cannot conclusively confirm the existence of an impedance imbalance between electrode pairs because we obtained the tissue-electrode impedance using a 2-point measurement configuration, which measures only the combined impedance of both electrode couplings together with the tissue and does not permit discrimination between one electrode and the other. Such discrimination would require a 3-point measurement configuration or equivalent, which measures the potential relative to a non-current-carrying electrode and thus allows one electrode at a time to be represented. However, the fact that impedance imbalances, in general, do exist between the tissue-electrode interfaces of different electrodes, and that such imbalances do result in noise being interpreted as a differential-mode signal, have been well described by Merletti *et al.* [18]; thus it is quite reasonable to assume that such imbalances were present

المنارة للاستشارات
www.manaraa.com

in our experiments and provided opportunity for phase errors to introduce noise into our recordings.

These conclusions are also supported by the results of the external noise immunity test. As shown in the example recording, in the case of the abrasive preparations only a slight increase in the noise floor is observed when the noise source is turned on, whereas in the case of the non-abrasive preparations the sEMG signal nearly disappears in the noise. The statistical results also bear this out: more abrasive preparations result in a much higher level of immunity to the induced noise. We thus conclude that abrasive preparation methods result in a much more robust tissue-electrode coupling. Indeed, the robustness of the abrasive preparations was also observed to apply to mechanical perturbations such as jerking on electrode wires or tapping the electrodes.

5.5 Conclusion

The effects of skin preparation methods on the impedance of the tissue-electrode interface and the signal-to-noise ratio of sEMG recordings have been systematically quantified and compared in human subjects. The only effect that was demonstrated to be significant is surface abrasion of the skin. Other effects, such as hair removal and alcohol cleaning, were not found to significantly affect either the impedance or the SNR. Further investigation with a larger number of participants may be helpful to confirm these results and to search for possibilities of effects that may be hidden in experimental variability. Nevertheless, it is clear from the present results that the overwhelming majority of the variability in both impedance and SNR across preparation methods is due to the presence or absence of surface abrasion in the preparation. Therefore, we recommend that abrasion be considered an essential component of skin preparation prior to placement of surface electrodes for sEMG and other recordings of small bioelectric surface potentials.

المنارة للاستشارات
www.manaraa.com

6. SUMMARY

The aims of the current work were (1) to complete the development of a set of tools for rapid, simple, and reliable full-spectrum characterization and Cole model analysis of the complex impedance of the tissue-electrode interface, and (2) to characterize the interfacial impedance and signal-to-noise ratio at the surface of the skin across a variety of preparation methods and test the hypothesis that surface abrasion is the principal determining factor in skin preparation to achieve consistently low-impedance, low-noise recordings.

With respect to the preliminary aim, while additional improvements to the toolset can certainly be made, a fully functional and up-to-date system for broadband impedance characterization has been achieved. Significant advances in stability, robustness, and ease of use have been realized. The hardware is small, portable, and battery powered, and features standard BNC jacks for easy connection to recording hardware. The software runs on a standard PC platform equipped with MATLAB, the LabVIEW runtime engine, and compatible acquisition hardware, which are typical in biosignal research environments.

For the second and primary aim, the skin-electrode interfacial impedance was successfully characterized, modeled, and compared pairwise among preparation methods; the signal-to-noise ratio was also measured and compared pairwise among preparation methods. We found our hypothesis to be strongly supported by the results: the degree of surface abrasion was the only factor that could be correlated to significant differences in either the interfacial impedance or the SNR. Within the group of three non-abrasive preparations, no significant differences were found in either impedance or SNR. Within the group of three abrasive preparations, no significant difference was found in impedance. A significant difference ($p = 0.014$) was found in SNR between sandpaper and razor shave; however, this still supports the hypothesis because (1) it is reasonable to assume that shaving is less abrasive than rubbing with sandpaper, and thus it is not surprising that the SNR would be

المنارة للاستشارات
www.manaraa.com

somewhat lower; and (2) the SNR for the razor-shave preparation was still significantly higher ($p = 0.007$) than for any of the non-abrasive preparations.

Given such clear and unambiguous results, we believe that abrasion holds the key to consistently obtaining a low-impedance contact interface and high-quality biopotential recordings. As lately as two years ago, a review editorial on bioelectric signal detection lamented that many years of research have failed to produce a comprehensively satisfactory solution in the quest for low-noise bioelectric recording methods [26]. While admittedly the experiments conducted in the present study were somewhat simplistic from a recording perspective — we did not attempt to record from EMG electrode arrays or other more complex scenarios cited in the aforementioned editorial — the proof of principle in our results is so undeniable that it nevertheless provides hope that a comprehensive solution may not be far away. We believe that a return to the reliability of abrasive preparations represented in the literature from past decades (as discussed in the introduction), and emphatically confirmed in the present experiments, is the first step to approaching more complex recording scenarios.

In the introduction, the question of whether noise contamination should be interpreted in terms of instrumentation technology rather than bioimpedance was briefly discussed. We now return to this question in light of the results of our experiments. Clearly, the tissue-electrode coupling is a significant contributor to the noise character of the recordings, as demonstrated by the fact that we achieved more than 300% increase in SNR simply by abrading the skin while using exactly the same recording circuit. The question that now remains is: why? How is it that the condition of the tissue-electrode interface can still wield such a significant degree of influence in a recording circuit with high input impedance and CMRR? There are a couple of possible explanations.

First, the most likely path that the noise still has available into the recording circuit is via unbalanced impedance between the two electrodes. It is instructive to examine the filtering characteristics of the tissue-electrode interface (see Figure 5.3(a)). Notice in particular that the maximum rate of change in phase for high-impedance skin is located near the 50–60 Hz range of power line noise. This maximizes the phase error of unbalanced impedances at

المنارة للاستشارات
www.manaraa.com

these frequencies, which could lead to selective inclusion of the 50-Hz power line noise and other noise in this frequency range.

The other explanation is that elimination of poor amplifier characteristics by technological advances have now left the tissue-electrode interface as the most significant source of error in the system. In other words, the tissue-electrode coupling is now the "weakest link" in the recording chain. This, we argue, is not a reason to ignore the tissue effect but rather to address it. Instead of relying only on better amplifier technology to make the best of the situation, let us address directly what now seems to be the largest contributor to noise in the recording system.

The results of the present experiments have confirmed systematically what was previously known empirically: that the low tissue-electrode impedance guaranteed by surface abrasion consistently provides an environment for reliable biopotential recordings. Although an alternative non-abrasive method involving controlled poration of the outer skin layer via ultrasonic energy has recently been successfully demonstrated to reduce interfacial impedance at low frequencies [27], such technology has not yet come into widespread use, perhaps due to cost. Until a reliable and economical substitute is demonstrated to nullify the high-impedance effects of the stratum corneum to a similar extent effected by abrasion, we maintain that abrasion should be considered an essential component of proper skin preparation prior to attachment of electrodes for recording of small bioelectric surface potentials.

المنارة للاستشارات
www.manaraa.com

LIST OF REFERENCES

المنارة للاستشارات
www.manaraa.com

LIST OF REFERENCES

[1] J. C. Williams, J. A. Hippensteel, J. Dilgen, W. Shain, and D. R. Kipke, "Complex impedance spectroscopy for monitoring tissue responses to inserted neural implants," *Journal of Neural Engineering*, vol. 4, no. 4, p. 410, 2007.

[2] K. S. Cole, "Electric impedance of suspensions of spheres," *The Journal of General Physiology*, vol. 12, no. 1, pp. 29–36, 1928.

[3] K. S. Cole, "Electric impedance of suspensions of Arbacia eggs," *The Journal of General Physiology*, vol. 12, no. 1, pp. 37–54, 1928.

[4] H. Fricke and S. Morse, "The electric resistance and capacity of blood for frequencies between 800 and $4\frac{1}{2}$ million cycles," *The Journal of General Physiology*, vol. 9, no. 2, pp. 153–167, 1925.

[5] K. S. Cole, "Electric phase angle of cell membranes," *The Journal of General Physiology*, vol. 15, no. 6, p. 641, 1932.

[6] K. S. Cole, "Permeability and impermeability of cell membranes for ions," *Cold Spring Harbor Symposia on Quantitative Biology*, vol. 8, pp. 110–122, 1940.

[7] D. H. Gordon, "Triboelectric interference in the ECG," *IEEE Transactions on Biomedical Engineering*, vol. BME-22, pp. 252–255, May 1975.

[8] H. W. Tam and J. G. Webster, "Minimizing electrode motion artifact by skin abrasion," *IEEE Transactions on Biomedical Engineering*, vol. BME-24, pp. 134–139, Mar. 1977.

[9] H. M. Hanish, R. A. Neustein, C. C. Van Cott, and R. T. Sanders, "Technical aspects of monitoring the heart rate of active persons," *The American Journal of Clinical Nutrition*, vol. 24, no. 9, pp. 1155–1163, 1971.

[10] P. A. Lynn, "Direct on-line estimation of muscle fiber conduction velocity by surface electromyography," *IEEE Transactions on Biomedical Engineering*, vol. BME-26, pp. 564–571, Oct. 1979.

[11] D. P. Burbank and J. G. Webster, "Reducing skin potential motion artefact by skin abrasion," *Medical and Biological Engineering and Computing*, vol. 16, no. 1, pp. 31–38, 1978.

[12] J. G. Webster, "Reducing motion artifacts and interference in biopotential recording," *IEEE Transactions on Biomedical Engineering*, vol. BME-31, pp. 823–826, Dec. 1984.

[13] H. J. Hermens, B. Freriks, C. Disselhorst-Klug, and G. Rau, "Development of recommendations for SEMG sensors and sensor placement procedures," *Journal of Electromyography and Kinesiology*, vol. 10, no. 5, pp. 361–374, 2000.

المنارة للاستشارات
www.manaraa.com

[14] H. W. Tam and V. E. Modes, "Skin preparation device and method used in the application of medical electrodes." Patent, June 1981. US 4274419 (assigned to Quinton Instrument Co.).

[15] Neuhaus Laboratories, *Owners Manual, T-2 Integrated Vacuum Tube Amplifier*.

[16] J. G. Webster, *Medical Instrumentation: Application and Design*. Hoboken, NJ: John Wiley & Sons, 4th ed., 2010.

[17] Burr-Brown Corporation, *High Speed FET-Input Instrumentation Amplifier*, 1992.

[18] R. Merletti, A. Botter, A. Troiano, E. Merlo, and M. A. Minetto, "Technology and instrumentation for detection and conditioning of the surface electromyographic signal: State of the art," *Clinical Biomechanics*, vol. 24, no. 2, pp. 122–134, 2009.

[19] K. Yoshida, A. Inmann, and M. K. Haugland, "Measurement of complex impedance spectra of implanted electrodes," in *Proceedings of the 4th Annual Conference of the International Functional Electrical Stimulation Society*, pp. 267–269, 1999.

[20] E. T. McAdams and J. Jossinet, "Tissue impedance: a historical overview," *Physiological Measurement*, vol. 16, pp. A1–A13, 1995.

[21] S. Grimnes and Ø. G. Martinsen, *Bioimpedance and Bioelectricity Basics*. New York: Academic Press, 2nd ed., 2008.

[22] J. Rosell, J. Colominas, P. Riu, R. Pallas-Areny, and J. G. Webster, "Skin impedance from 1 Hz to 1 MHz," *IEEE Transactions on Biomedical Engineering*, vol. 35, pp. 649–651, Aug. 1988.

[23] K. Blake, *Op Amp Precision Design: PCB Layout Techniques (Application Note AN1258)*. Microchip Technology Inc., 2009.

[24] Ø. G. Martinsen, S. Grimnes, and E. Haug, "Measuring depth depends on frequency in electrical skin impedance measurements," *Skin Research and Technology*, vol. 5, no. 3, pp. 179–181, 2006.

[25] D. C. Montgomery, *Design and Analysis of Experiments*. Hoboken, NJ: John Wiley & Sons, 7th ed., 2009.

[26] R. Merletti, "The electrode–skin interface and optimal detection of bioelectric signals," *Physiological Measurement*, vol. 31, no. 10, 2010.

[27] A. Farinha, S. Kellogg, K. Dickinson, and T. Davison, "Skin impedance reduction for electrophysiology measurements using ultrasonic skin permeation: initial report and comparison to current methods," *Biomedical Instrumentation & Technology*, vol. 40, no. 1, pp. 72–77, 2006.

[28] D. Brodie, V. Moscrip, and R. Hutcheon, "Body composition measurement: a review of hydrodensitometry, anthropometry, and impedance methods," *Nutrition*, vol. 14, no. 3, pp. 296–310, 1998.

[29] G. E. Loeb and C. Gans, *Electromyography for Experimentalists*. Chicago: The University of Chicago Press, 1986.

المنارة للاستشارات
www.manaraa.com

[30] R. B. Stein, D. Charles, T. Gordon, J.-A. Hoffer, and J. Jhamandas, "Impedance properties of metal electrodes for chronic recording from mammalian nerves," *IEEE Transactions on Biomedical Engineering*, vol. BME-25, pp. 532–537, Nov. 1978.

[31] J. C. Williams, R. L. Rennaker, D. S. Pellinen, and D. R. Kipke, "Time-varying changes in complex tissue impedance immediately following local insult with arrays of chronic microelectrodes in auditory cortex," in *Proceedings of the Society for Neuroscience Annual Meeting*, 1998.

[32] Y. Yamamoto, T. Yamamoto, S. Ohta, T. Uehara, S. Tahara, and Y. Ishizuka, "The measurement principle for evaluating the performance of drugs and cosmetics by skin impedance," *Medical and Biological Engineering and Computing*, vol. 16, pp. 623–632, 1978.

[33] R. B. Stein, R. Rolf, and B. Calancie, "Improved methods for studying the mechanical properties of biological systems with random length changes," *Medical and Biological Engineering and Computing*, vol. 24, no. 3, pp. 292–300, 1986.

[34] W. Press, B. Flannery, S. Teukolsky, and W. Vetterling, *Numerical Recipes in C: The Art of Scientific Computing*. Cambridge University Press, 2nd ed., 1992.

المنارة للاستشارات

www.manaraa.com

APPENDICES

المنارة للاستشارات
www.manaraa.com

A. RAPID MEASUREMENT OF COMPLEX IMPEDANCE SPECTRA OF ELECTRODES

Abstract

We have developed a method of quickly determining the complex impedance spectra. A broadband current waveform was injected through the test electrode. The injected current and resulting voltage waveforms were sampled and the transfer functions of these waveforms were digitally calculated to determine the complex impedance spectrum. The approach was applied to known linear devices as resistors and RC networks as a validation of the method and tested with gel-type surface electrodes and implanted electrodes in an acute animal preparation. Two types of broadband waveforms were tested: bandwidth limited noise and frequency sweep. Comparisons were made between our new method to measurements made using pure tones. We found that the technique was able to successfully measure the complex impedance of purely resistive and RC networks using either test waveform.

A.1 Introduction

The measurement of electrode impedance is a common method to noninvasively assess the continuity and condition of chronically implanted electrodes in humans and in animal models. The impedance spectrum used with 3- or 4-point electrode configurations can isolate the condition of the electrode contact, or the tissues between the electrodes. Similar to impedance-based body composition measurement [28], electrode impedance spectroscopy (EIS) can be used to identify the differential frequency dependencies of various tissues, which can be leveraged to identify changes in tissue types or electrode encapsulation [1].

المنارة للاستشارات
www.manaraa.com

At present, EIS is not a practical measurement technique because of the need of relatively complex instrumentation and time required to conduct the test. Instead, a standard technique is to pass a small amplitude (~1 μA), constant current, 1 kHz sine wave through the electrode and measure the peak-to-peak amplitude of the voltage [29, 30]. Simple division of the measured voltage amplitude by the amplitude of the injected current gives the magnitude of the electrode impedance at this particular frequency. The phase information is typically not used, and impedance values at other frequencies are not considered.

However, the processes involved at the tissue-electrode interface are complex and not purely resistive. Moreover, changes to this interface or to the tissue by biological processes may express themselves as distributed changes in the impedance spectrum. In fact, Williams *et al.* [31] have shown evidence that the real component of the complex impedance may correlate to physiological changes in the tissue-electrode interface of chronically implanted wire intracortical electrodes. In order to adequately investigate these complex phenomena, it is necessary to obtain a broad spectrum of the complex impedance.

The primary factor limiting the use of EIS is the difficulty in making the measurements. Obtaining a broad spectrum of the complex impedance using instruments designed for single-frequency measurements is often a laborious and time-consuming process. In contrast, when measuring electrode impedances in awake animals, measurements must be made quickly and easily. One is often limited to less than 5 seconds per electrode — not nearly enough time to measure impedance at multiple frequencies one at a time. To address these difficulties, we have developed a method of quickly measuring complex electrode impedance spectra between the two test poles of our device. In this paper we present the method and discuss its accuracy and its application to the measurement of implanted nerve electrodes.

The characterization of skin impedance spectrum has been used in other applications. Small changes in the skin impedance have been used to monitor the effect of cosmetics and moisturizers on human skin [32]. The skin presents itself as a high-impedance electrical barrier, which impedes efficient stimulation of muscles using surface stimulation and decreases the quality of surface electromyogram (EMG) and electrocardiogram

المنارة للاستشارات
www.manaraa.com

(ECG) recordings. The high-impedance layer of the skin is the uppermost layer, the stratum corneum [16]. Methods to break down this high-impedance layer by abrading the skin and/or using various gels is an important consideration in preparing to record from or stimulate underlying tissues, and is discussed in more detail in previous chapters.

Whether the impedance associated with recording and/or stimulation is located at the skin or elsewhere, characterization of such impedance over a wide spectrum of frequencies is essential to the reliability of the transmitted signals. The method presented in this paper allows us to quickly characterize the impedance using a using a relatively simple apparatus.

A.2 Methods

A.2.1 Technique

Bandwidth-limited noise (0.1 Hz–13 kHz) was applied through a custom-built voltage-controlled current source to produce a low-amplitude current excitation waveform ranging from ~100 nA to ~100 μA depending on the application. The excitation current was injected through the test electrode while both the injected current and the resulting voltage waveforms were digitally sampled for 10 seconds at 30 kHz. The offsets of the sampled waveforms were digitally removed and the samples were passed through a Hann window of the same length before calculating their Fast Fourier Transforms. The impedance spectrum of the electrode was derived by taking the complex Fourier coefficients of the voltage waveform and dividing by those of the current waveform. The phase skewness due to the non-instantaneous sampling of the two data channels was corrected by subtracting from the measured phase the linear phase corresponding to the interchannel sampling delay. The impedance coefficients, which are distributed linearly with frequency, were grouped into logarithmically sized bins and averaged to reduce the error of the spectrum at higher frequencies and to evenly distribute points logarithmically with frequency [33]. The data were sampled through a 12-bit A/D board (NI PCI-MIO-16E-4, National Instruments, Austin, TX, USA) and analyzed using a custom LabVIEW-based application.

المنارة للاستشارات
www.manaraa.com

A.2.2 Testing and Validation

A set of calibrated resistors [100M 10M 1M 100k 10k 1k 100 10] and capacitors [10u 1u 100n 10n 1n] were used to assess the accuracy of the measurements made with the device. The resistors were calibrated using a multimeter (HP34401A) after nulling for the test lead impedance. The capacitors were calibrated using an LCR meter (Escort ELC-131D) using its socket test contacts. These calibrated resistors and capacitors were used to test the precision and accuracy of the impedance device.

The technique was tested on purely resistive and capacitive impedances and then a simple RC filter to determine if it would be able to successfully measure their spectral impedances. Following the test on simple linear components, the method was applied to cuff electrodes both isolated in saline and implanted in the peripheral nerve.

Noise vs pure tone

The rapid Z method was tested in comparison with pure tone measures. In the rapid Z method, bandwidth-limited noise was used as the excitation waveform. In the pure-tone tests, fixed-amplitude sinusoids of 1, 10, 100, 1k, and 10k Hz digitally synthesized by a function generator (Philips PM5138) were used as the excitation waveform. Sinusoids were 3.45 μA_{pp}. Noise stimuli were 10 μA_{pp}. The excitation waveform was routed to the input of a custom-built potentiostat/galvanostat running in galvanostat mode. The device precisely converts the input voltage waveform into a current, with three user-selectable transconductance gains (1, 10, and 100 $\mu A/V_{in}$). The output current and the voltage drop across the unknown load are both measured. The current sense has three user-selectable transresistance gains (1, 10, and 100 $\mu A/V_{out}$), and the voltage sense has three user-selectable voltage gains (1, 0.1, and 0.01 V/V_{out}). These sense output gains allow bracketing the range of the device to maximize the resolution and signal-to-noise ratio of the acquisition system. Measurements, in all cases, consisted of a 10–20 s epoch of the voltage and current waveforms digitally sampled and stored to PC using a 12-bit data acquisition card (National Instru-

المنارة للاستشارات
www.manaraa.com

ments, PCI-E series). The data were pseudo-simultaneously sampled with an interchannel delay of 4 µs at a sampling rate of 25.4 kS/s per channel.

For each test condition, the amplitude, phase, and frequency of the pure-tone voltage and current were estimated by fitting the parameters of the captured voltage and current sinusoid using the Levenberg-Marquardt nonlinear recursive fit algorithm [34]. The impedance gain for each test frequency was calculated by dividing the estimated voltage amplitude by that of the current amplitude. The phase was estimated by subtraction of the current phase from the voltage phase. Errors of the fit derived from the L-M fit were used as the estimate of the variance of the measure. For comparison with the noise method at each pure tone, the impedance value from the nearest frequency from the noise derived impedance measurement was used. Since the hardware used to make the measurement is the same, the pure tone measurement serves as a test of the accuracy of the noise-based measurement technique.

Resistors

The resistance for the calibrated resistor set was assumed to be constant in the frequency range between 0.1 Hz and 20 kHz. The set of resistors were used to test the range and accuracy of the noise-based impedance technique. The absolute value of the relative error between the resistor value and the measured value was quantified and plotted. This process was tested with and without compensation for the parasitic lead capacitance (see Appendix B) and both sets of results are shown.

Capacitors

Similar to the resistor test, the calibrated capacitor set was tested with the noise-based method. The measured impedance values were converted to equivalent capacitance values (see Appendix B for details) so that the resulting magnitude plots would be flat across frequency, similar to the impedance profile of a resistor. As before, the process was tested with and without parasitic capacitance compensation, and both sets of results are shown.

المنارة للاستشارات
www.manaraa.com

RC circuit

Since resistors contain only real impedance, and capacitors (theoretically) only imaginary, the method was also tested with a linear RC circuit (10 kΩ parallel to 0.1 μF) to validate against a known complex impedance spectrum. In this test, a frequency-sweep input was also provided to the measurement device for comparison with the noise method. Both outputs were plotted along with the theoretical impedance spectrum.

Cuff electrodes

In addition to testing the accuracy and precision of the method on linear circuits, we also measured the impedance of multi-contact cuff electrodes both in isolation and in a biological environment. The purpose of this testing was to demonstrate that the impedance of electrodes and biological tissue can be measured by this method even though they do not behave as linear systems.

In vitro: saline solution Electrodes were placed in a 0.9% saline solution at 37 °C and the impedance between contacts was measured. An example impedance spectrum is plotted in Figure A.2.

In vivo: peripheral nerve Electrodes were implanted in an acute preparation around the sciatic nerve of an anesthetized rabbit. A typical example of an impedance spectrum from the implanted cuff is shown in Figure A.3.

A.3 Results

The complex impedance spectrum of purely resistive components and simple RC networks were reliably resolved using the described method. A typical example of a spectrum from the simple RC filter is shown in Figure A.1.

The largest errors occur at the low-frequency end because of the inherent limitations of the FFT algorithm estimation imposed by the duration of the recording. Errors also tend

المنارة للاستشارات
www.manaraa.com

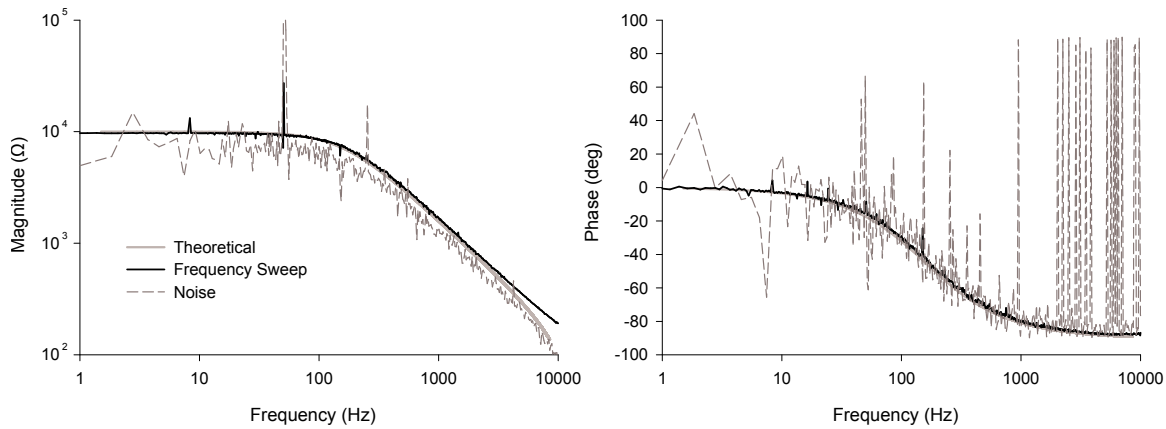

Figure A.1. Magnitude and phase of impedance recorded from a simple RC filter (10 kΩ || 0.1 μF) using two modes of broad bandwidth current, frequency sweep (black) and broad bandwidth noise (dashed). These are shown compared to the theoretical curves (gray).

to be high for large resistances at high frequencies due to the internal capacitance of the system.

Both types of broad bandwidth excitation, frequency sweep and noise, resulted in resolution of the complex impedance spectrum and were comparable to those predicted mathematically for the linear RC network. The impedance spectra characterized by the frequency sweep were generally cleaner than those characterized by broad bandwidth noise. Broad bandwidth noise characterized impedances also showed greater phase error, especially at frequencies approaching 10 kHz.

In the calibrated resistor test, the noise-based technique was shown to accurately measure the resistor values from 100 Ω to 1 MΩ without compensation for the parasitic capacitance. With compensation, values as high as 100 MΩ could be resolved. The measured impedance profiles, both before and after compensation, are plotted together in Figure A.4.

For large resistances, the effect of parasitic capacitance can be seen in the divergence of each pair of curves moving toward higher frequencies. Compensation broadens the span over which the curve remains flat, thus allowing the fidelity of the impedance measurement to be extended over a wider frequency range. At the low-resistance end, values as low as

المنارة للاستشارات
www.manaraa.com

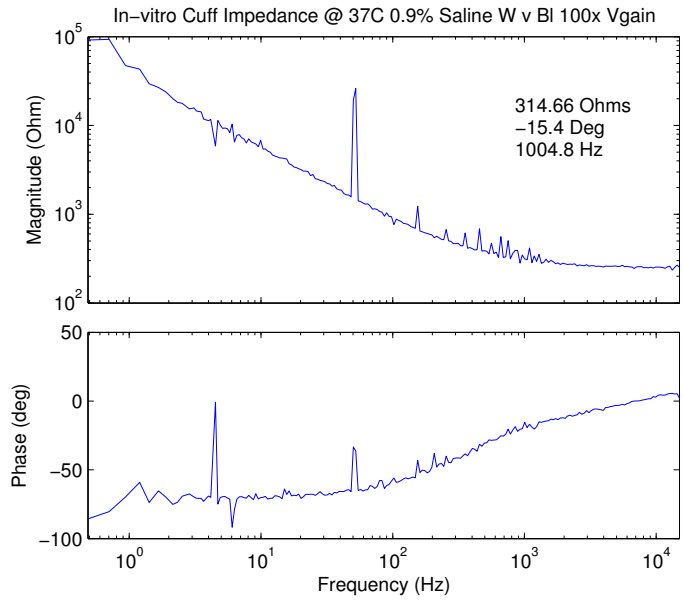

Figure A.2. Magnitude and phase of the impedance recorded from a cuff electrode in saline using the noise method.

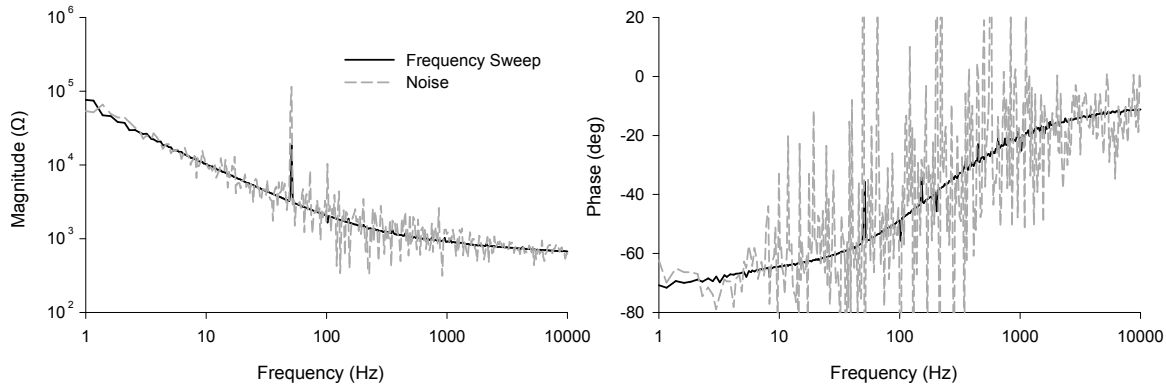

Figure A.3. Magnitude and phase of the impedance recorded from a cuff electrode implanted acutely around the sciatic nerve of an anesthetized rabbit. Impedance was characterized using both modes of broad bandwidth current, frequency sweep (black) and broad bandwidth noise (dashed).

100 Ω could be reliably measured, and even the 10 Ω resistor was approximately resolved. Values less than 10 Ω fell below the noise floor and could not be resolved.

المنارة للاستشارات
www.manaraa.com

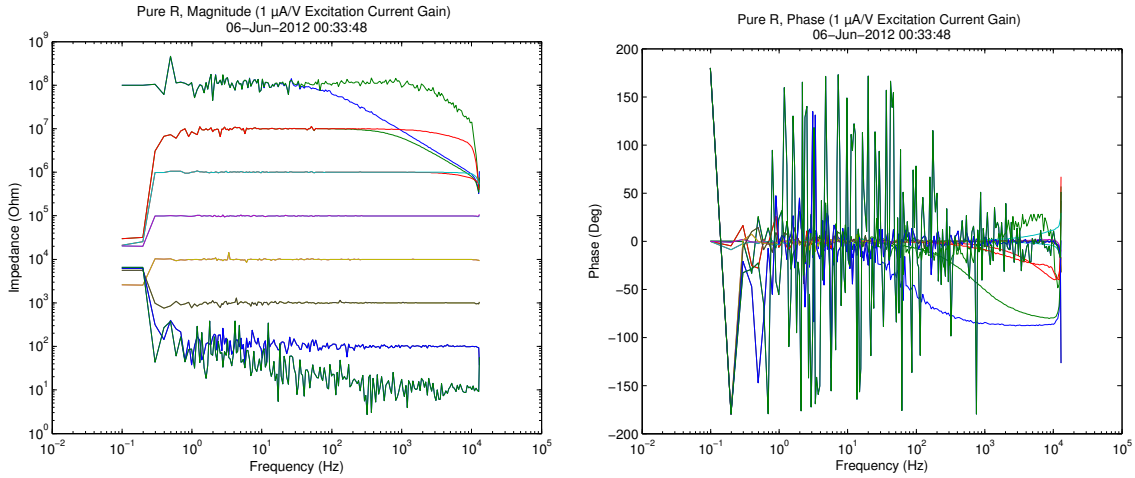

(a) Magnitude (b) Phase

Figure A.4. Frequency profiles of impedance recorded from the calibrated resistor set. The dominance of the parasitic capacitance at higher impedances and frequencies is demonstrated by the divergence of compensated and uncompensated profile pairs and the convergence of all uncompensated profiles to the same asymptote as frequency increases.

The quantified errors in the resistance measurements are plotted as a colormap against impedance and frequency as shown in Figure A.5. The largest errors occur at the low-frequency end because of the inherent limitations of the FFT algorithm estimation imposed by the duration of the recording. Errors also tend to be high for large resistances at high frequencies due to the internal capacitance of the system.

Finally, in the calibrated capacitor test, values were reliably resolved from 1 nF to 10 μF using the noise input. Over this capacitance range, the contribution of the parasitic internal capacitance is negligible; thus, although both compensated and uncompensated curves were plotted (Figure A.6), virtually no difference is discernible.

A.4 Discussion

Measurements can be made to tape, and analysis done offline. Since there is no need to synchronize to the noise waveshape, the analysis can be scaled in time to suit the bandwidth

المنارة للاستشارات
www.manaraa.com

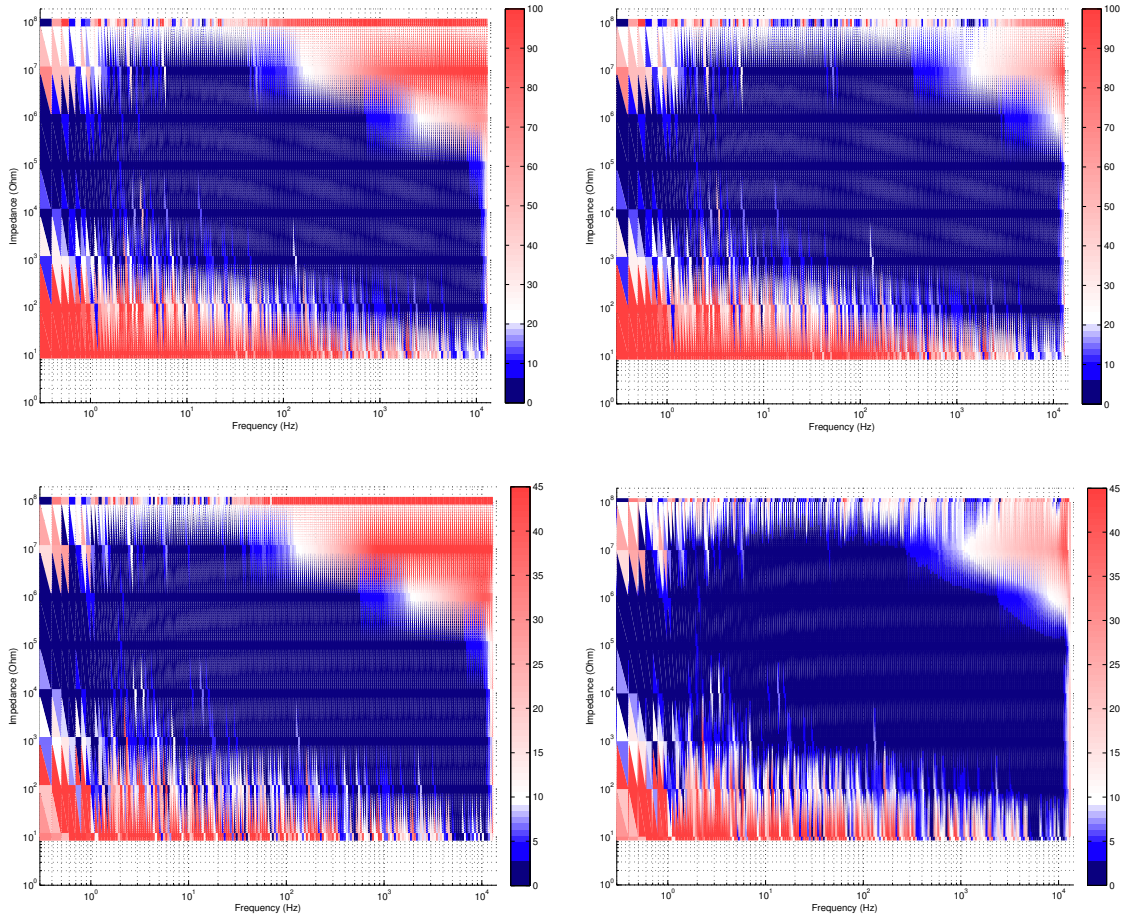

(a) Error before compensation for parasitic capacitance.

(b) Reduced errors after capacitance compensation is applied.

Figure A.5. Colormaps showing relative percent errors in measurements of impedance magnitude (top) and phase (bottom), as a function of impedance and frequency for the calibrated resistor set.

of interest. Noise is easy to produce. The method requires very well tuned antialiasing filters. Method is somewhat computationally intensive, but is made possible by the high speed processors available today. Speed of computation will decrease with the increasing horsepower of CPUs in the future.

Transfer function estimation using pointwise division of Fourier coefficients is a promising method for quickly determining the complex impedance of implanted electrodes. The principal advantage of the method is that a more continuous impedance spectrum can

المنارة للاستشارات
www.manaraa.com

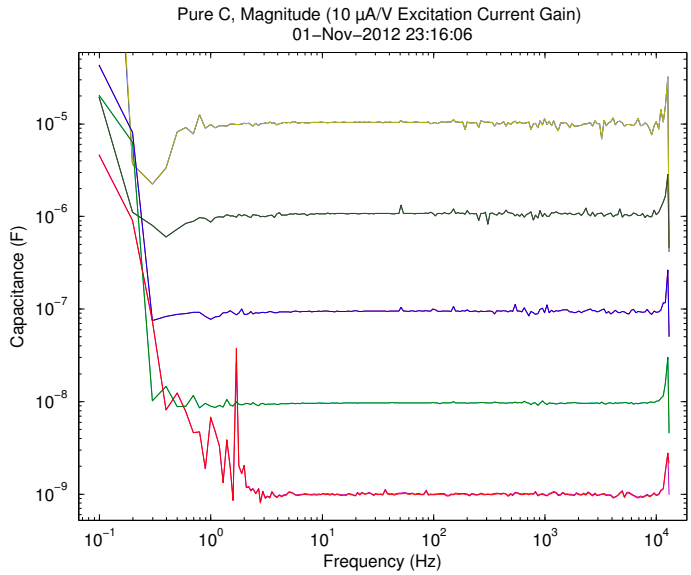

Figure A.6. Frequency profiles of capacitance recorded from the calibrated capacitor set.

be generated, consisting of hundreds or thousands of frequency points based on a single 20–30 s sampling. We found that the shape and features of the theoretical impedance of the linear components and the complex electrode impedance from literature based on multiple single frequency measurements were generally well reproduced using this method.

The successful implementation of the method hinges on the use of broadband excitation to ensure that there is sufficient energy in the excitation waveform at all frequencies within the range of the impedance characterization. We tested two different modes of this broadband excitation, frequency sweep and broadband noise, and found that frequency sweep excitation resulted in cleaner and faster characterization of the complex impedance spectrum. There was considerable error and chatter in the impedance spectra derived based on broad bandwidth noise excitation. Although its performance was poorer than the frequency sweep excitation mode, broadband noise excitation has one significant advantage: it is simple to generate, and thus can be easily implemented in hardware. The accuracy of the transfer function estimation can be improved by increasing the duration of the sampling period or decreasing the frequency range of the spectrum to be characterized to increase the number of spectra averaged using Welch's method of spectral averaging. In addition,

المنارة للاستشارات
www.manaraa.com

it should be noted that the measurements taken in this study were obtained from early implementations of the measurement system; more recent revisions have resulted in cleaner spectral impedance characterizations from the broadband noise method.

Although the method was tested using bandwidth limited noise, other waveforms could be used, such as frequency sweeps, as long as they contain power in the spectrum of analysis. More interesting, since stimulation waveforms have spectral power in the frequency range, bandwidth limited stimulation voltage and currents could be sampled to determine and monitor the impedance during stimulation, as long as the stimulus strength is kept below the nonlinear threshold of the electrode interface.

The basic rationale for exploring complex impedance spectrum was to determine whether it is possible to evaluate the condition of the tissue-electrode interface and that of the implanted tissue based on a simple noninvasive measurement. Looking towards future work, we intend to take this method and test it in the chronic animal model to determine whether the effects seen by Williams *et al.* with cortical electrodes have similar correlates with peripheral nerve electrodes. It remains to be seen if less selective peripheral nerve electrodes will be able to resolve the local effects seen with intracortical electrode arrays. Nonetheless, the rapid measurement of the complex impedance spectrum is itself an important development because it offers the possibility of parametric value estimation of components in a mathematical model of the electrode and surrounding tissue.

A.5 Conclusion

A method for rapid measurement of the complex impedance spectrum of electrodes has been demonstrated and validated both theoretically and *in vivo*. The method requires a means to generate the noise, a galvanostat or potentiostat, and a means to sample the excitation waveform and the resultant current or voltage waveform across the load impedance. Other than a PC, no additional equipment is needed. The hardware is simplified compared to other methods of generating wide-spectrum signals. It is small, portable, and battery powered, and can be easily coupled to the PC for data logging and online real-time analy-

المنارة للاستشارات
www.manaraa.com

sis. The successful demonstration of this method opens the possibility of a wide variety of applications for rapid EIS characterization of biological tissues and electrode interfaces.

المنارة للاستشارات
www.manaraa.com

B. CALIBRATION AND COMPENSATION FOR LEAD WIRE PARASITIC CAPACITANCE

Abstract

Complex impedance measurements contain inherent distortion due to the internal capacitance of the measurement system, particularly from the electrode lead wires. We have developed a straightforward method for calibration and compensation for such parasitic capacitance distortion. The method involves modeling the open-circuit impedance of the recording system as primarily capacitive, then calculating its dominant capacitance value and finally using the capacitance in linear circuit models to compensate the original impedance measurements. The method is easily implemented in software used post-hoc, and was found to increase the valid measurement range of the device by approximately one decade in either the frequency scale or the impedance scale.

B.1 Introduction

In any measurement apparatus, the possibility of distortion effects due to the measurement instrument itself must be considered. In the case of measuring complex impedances, if the load impedance to be measured is relatively low, the effect of the parallel capacitance of the electrode lead wires through the air is typically small and can often be ignored. However, when the load impedance is high, the parasitic effect of the lead wire capacitance can substantially distort the impedance measurement, especially at high frequencies. This could be quite detrimental if the higher-frequency characteristics of the system under measurement are of interest. We have developed a method for calibration and compensation for the distortion of complex impedance measurements due to the parasitic capacitance of

المنارة للاستشارات
www.manaraa.com

electrode lead wires. The method is straightforward, uses data taken by the measurement system itself, and is implemented post-hoc in software used offline.

In order to compensate for the parasitic capacitance, we first quantify it independently by measuring its impedance in isolation and modeling the impedance as a pure capacitance. The impedance Z_C of such an ideal capacitance C is given by

$$Z_C = \frac{1}{j\omega C} \tag{B.1}$$

and thus we can solve for C:

$$C = \frac{1}{j\omega Z_C} \tag{B.2}$$

Now, since Z_C is purely imaginary, $Z_C = j\,\Im(Z_C)$ and thus

$$\begin{aligned} C &= \frac{1}{j\omega[j\,\Im(Z_C)]} = \frac{1}{j^2\omega\,\Im(Z_C)} \\ &= \frac{-1}{\omega\,\Im(Z_C)} \end{aligned} \tag{B.3}$$

Theoretically, the expressions for capacitance in Equations (B.2) and (B.3) are equivalent; however, Equation (B.3) is preferred for computation. This is because the actual data for Z_C will inevitably contain nonzero real parts due to inexact measurements and/or rounding errors. Explicitly selecting only the imaginary parts simplifies the computation by allowing the resulting capacitance values to be handled as purely real numbers.

Once the parasitic capacitance is known, we assume it to be in parallel with the load impedance we wish to measure, and we use standard circuit relations to compensate for it. The equations are easier to construct if we begin with admittance and convert to impedance later. The admittance Y of a parallel circuit is the summation of the individual admittances, so we have

$$Y_m = Y_d + Y_p \tag{B.4}$$

where Y_m is the actual measured circuit admittance (contaminated by the parasitic capacitance), Y_d is the desired admittance to be measured, and Y_p is the equivalent admittance of the parasitic capacitance. We compensate by simply subtracting out Y_p:

$$Y_d = Y_m - Y_p \tag{B.5}$$

المنارة للاستشارات
www.manaraa.com

Then we invert both sides to convert to impedance and use Equation (B.1) to insert the parasitic capacitance C_p:

$$Z_d = \frac{1}{\frac{1}{Z_m} - \frac{1}{Z_p}} = \frac{1}{\frac{1}{Z_m} - j\omega C_p}$$
$$= \frac{Z_m}{1 - j\omega C_p Z_m} \tag{B.6}$$

Thus, given an independent measure of the parasitic capacitance C_p, we can correct any impedance measurement Z_m by using Equation (B.6). We have implemented the calculation of the capacitance and the compensation of impedance measurements as an automated procedure in MATLAB.

B.2 Technique

1. Obtain open-circuit broadband impedance spectrum of measurement apparatus including leads (*e.g.*, using the rapid impedance measurement technique given in Appendix A).
2. Search impedance phase values for frequencies where the phase angle is near $-90°$, discard other data, and convert remaining impedance values to equivalent capacitance values using Equation (B.3).
3. Calculate median of capacitance values (first approximation).
4. Discard values that lie more than 0.5 standard deviation away from the median.
5. Calculate median of remaining values (second approximation). Report median and standard deviation as final result.
6. Use the capacitance calculated in step 5 as the value for C_p in Equation (B.6) to compensate any future impedance measurements made with the given apparatus.

المنارة للاستشارات
www.manaraa.com

B.3 Validation

We tested the compensation algorithm with a set of calibrated decade resistors. Using the method in Appendix A, the impedance of each resistor and the open-circuit impedance of the measurement device were measured. The impedance of each resistor was plotted against frequency with and without compensation.

To demonstrate that the calibration algorithm selects the correct capacitance value from the open-circuit impedance data, a straight line corresponding to the calculated capacitance was plotted on the same graph with the open-circuit data after transformation to capacitance values.

B.4 Results

Since the impedance magnitude profile of a resistor is a straight line across all frequencies, and a parallel capacitance will cause a drop in impedance as frequency increases, the degree to which the "drop-off" at higher frequencies is removed becomes a measure of the efficacy of the compensation algorithm. Figure B.1 shows the results of the calibration and compensation processes. All uncompensated curves converge to the same linear asymptote as frequency increases, indicating the presence of the common parallel capacitance. For each corresponding curve after compensation, the flat portion of the curve is extended at the high-frequency end, indicating a substantial correction.

Comparing the three sets of impedance traces, it is clear that not all parasitic capacitance has been removed from the system, and that higher-impedance loads will still be difficult to characterize. However, in each case the corner frequency is moved to the left approximately one decade, and the corner frequency of each compensated trace roughly equals that of the uncompensated trace at the next higher impedance decade. This effectively increases the overall measurement range by one decade either in frequency or in impedance.

المنارة للاستشارات
www.manaraa.com

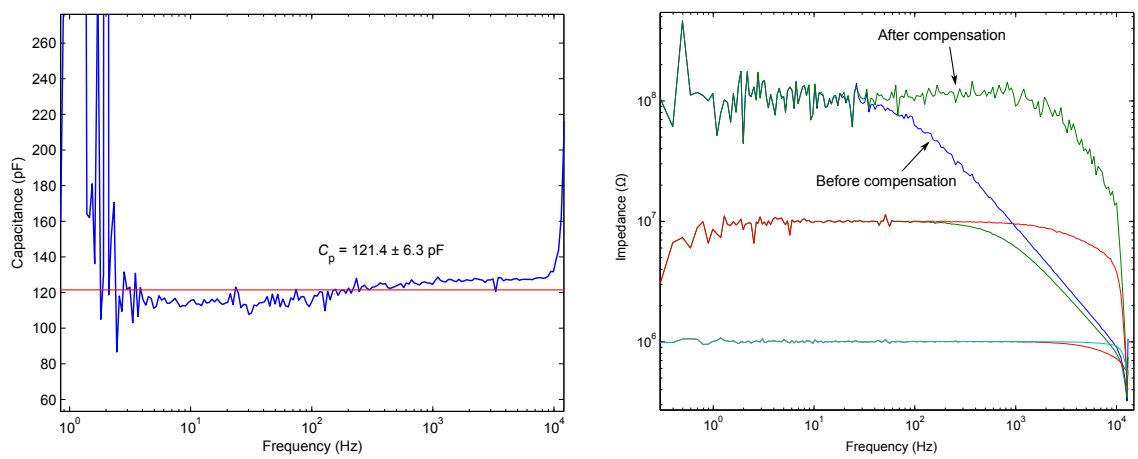

(a) Example parasitic capacitance estimated by calibration algorithm. The blue trace is the impedance data after conversion to capacitance.

(b) Measured impedance magnitude of decade resistors before and after compensation for the parasitic capacitance.

Figure B.1. Calibration and compensation performed by the described methods.

B.5 Discussion

Compensation for the parasitic capacitance of the measurement device allows the measurement of load impedances to be accurate over a wider range of frequencies and increases the overall reliability of the measurement. In addition, it increases the range of impedances over which valid measurements can be made. In the case of the 100 MΩ resistor, for example, the uncompensated impedance is barely resolvable and would require *a priori* knowledge to be recognized as a resistor, whereas in the compensated curve the flat characteristic dominates over most of the frequency range and is much easier to resolve.

The method requires no additional hardware or special configuration beyond what is used for obtaining normal impedance measurements. It only requires that one additional impedance reading be taken, namely the open-circuit impedance which can be obtained by merely disconnecting the leads from the measurement load. All compensation is done post-hoc in software. This allows measurements during an experiment to be taken more efficiently and without any special concerns, and also allows both compensated and uncompensated readings to be saved and analyzed separately if desired. Computation is straight-

المنارة للاستشارات
www.manaraa.com

forward and easily implemented. A partial limitation of the calibration computation is that the open-circuit impedance data typically contain a substantial number of outliers after conversion to capacitance, probably due to the nonlinear relationship between impedance and capacitance. To offset this difficulty, we used the median instead of the mean to select the capacitance value due to the superior outlier rejection properties of the median.

B.6 Conclusion

A simple method for calibrating an impedance measurement apparatus for the capacitance of its lead wires and applying post-hoc compensation to acquired data has been demonstrated and implemented in MATLAB. The method was shown to increase the range of resolvable impedance measurements by approximately one decade in either frequency or impedance.

المنارة للاستشارات
www.manaraa.com